

Hole subband dispersions and strong ‘spin’-orbit coupling in a cylindrical Ge nanowire

Rui Li (李睿) ^{1,*}

¹*Hebei Key Laboratory of Microstructural Material Physics,
School of Science, Yanshan University, Qinhuangdao 066004, China*

(Dated: September 27, 2024)

Quasi-one-dimensional hole gas is achievable in semiconductor nanowire structures. This paper briefly reviews both the calculation method and the low-energy effective description of the hole subband dispersions in a cylindrical Ge nanowire. Using the Luttinger-Kohn Hamiltonian in the axial approximation, two transcendental equations determining the subband dispersions are analytically derived. Subband dispersions for three representative growth directions [001], [111], and [110] are given. The lowest two subband dispersions are shown to be two shifted parabolic curves with an anticrossing at $k_z R = 0$. This peculiar low-energy subband structure manifests the existence of a strong ‘spin’ (pseudo spin)-orbit coupling, although each dispersion line is spin degenerate. Either a strong longitudinal or a strong transverse magnetic field is used to lift this spin degeneracy, such that two sets of combined dispersions modelled by a two-band Hamiltonian $H^{\text{ef}} = \hbar^2 k_z^2 / (2m_h^*) + \alpha \sigma^x k_z + g_h^* \mu_B B \sigma^z / 2$ are obtainable. These results are further confirmed via constructing the low-energy effective Hamiltonian of the hole gas, where the explicit expressions of α and g_h^* are also given.

I. INTRODUCTION

The valence bands of bulk semiconductors are composed of a heavy-hole, a light-hole, and a spin-orbit split-off bands [1–3]. These three bands overlap with each other in the valence bands. The heavy-hole and light-hole bands touch with each other at the valence band top, i.e., the Γ point of the Brillouin zone. The spin-orbit split-off band is separated from the heavy-hole and light-hole bands by a spin-orbit energy gap [4]. The effective Hamiltonian describing the valence bands near the Γ point was developed by Luttinger and Kohn [5]. When the spin degree of freedom is included, the Luttinger-Kohn Hamiltonian is a 6×6 matrix, which is complicated by itself even before its applications to the low-dimensional nanostructures [6–9]. Fortunately, when the spin-orbit energy gap is much larger than the other energy scales in the nanostructures, we can safely use the 4×4 Luttinger-Kohn Hamiltonian instead [10–13]. The 4×4 Luttinger-Kohn Hamiltonian describes the heavy-hole and light-hole bands only, and is regarded as a minimal bulk hole model [5, 14].

Holes in traditional quasi-two-dimensional semiconductor structures, such as metal-oxide-semiconductor structure [15], heterojunction [16–21], and quantum well [11, 12, 16, 22], were well studied (see also the reviews [23–25]). While holes in quasi-one-dimensional nanostructures have not attracted much attention, until recently their potential applications in field effect transistor [26] and spin quantum computation [27] were recognized. Quasi-one-dimensional hole gas can be achieved in various nanowire structures, such as Ge/Si core/shell nanowires [28], bare Ge hut wire [29], and bare InSb nanowire [27] etc. Note that current experiments mainly

used undoped nanowire, the two ends of which are connected to metal electrodes [30]. The nanowire can be populated with holes by a back gate, i.e., a p^{++} doped Si layer lying below the nanowire [30, 31].

Holes in the nanowire are allowed to move freely only in the longitudinal direction. In order to understand the various hole properties in quasi-one-dimension, the first step is to understand the hole subband dispersions caused by the size quantization of the nanowire. Using the Luttinger-Kohn Hamiltonian in the spherical approximation [14], Sercel and Vahala obtained the transcendental equation determining the hole subband dispersions as early as 1990 [32]. Sweeny et al. even gave an equivalent transcendental equation two years earlier using a coordinate free method [33]. In 2024, Li generalized these transcendental equations from the spherical approximation to the axial approximation [34]. The axial approximation is superior to the spherical approximation for it can describe the band anisotropy to some extent [35, 36]. Especially, the axial approximation is able to give rise to high accurate subband dispersions for both growth directions [001] and [111] [2].

The lowest two subband dispersions obtained are just two shifted parabolic curves with an anticrossing at $k_z R = 0$ [37–41]. This result indicates the hole gas is naturally strong ‘spin’ (pseudo spin)-orbit coupled, where the ‘spin’ is introduced to describe the two shifted directions of the parabolic curve [37, 40]. Note that each dispersion line is spin degenerate. Using a strong magnetic field to lift this spin degeneracy, we obtain two sets of combined dispersions, and each set is strong ‘spin’-orbit coupled [40]. The magnetic field can be applied either longitudinally or transversely. A strong transverse external electric field can also lift the spin degeneracy at $k_z \neq 0$ due to the Rashba effect [19, 37, 42–46], strong hole spin-orbit coupling, instead of ‘spin’-orbit coupling, is achievable in this case.

* ruli@ysu.edu.cn

The strong ‘spin’ or spin-orbit coupling achieved by either strong magnetic field or strong electric field has many potential applications. The strong ‘spin’ or spin-orbit coupling can be used to facilitate the hole spin manipulation in an oscillating electric field [47–51], to achieve the strong spin-photon interaction in a quantum-dot-cavity system [52–54], to achieve the topological superconductivity in a hybrid semiconductor-superconductor structures where Majorana modes are expected to exist at the two ends of the nanowire [55–57]. The spin relaxation induced by lattice phonons [58, 59] and the spin dephasing induced by charge noise [53] can also be mediated by this spin-orbit coupling.

This paper is organized as follows. In Sec. II, the Luttinger-Kohn Hamiltonian and its two approximated versions are introduced. In Sec. III, the symmetries of the effective mass Hamiltonian of the hole gas are discussed. In Sec. IV, the solutions to the bulk Hamiltonian are given. In Sec. V, we derive two transcendental equations by utilizing the bulk solutions. In Sec. VI, subband dispersions for three representative growth directions [001], [111], and [110] are given. In Sec. VII, spin splittings induced by external magnetic fields are calculated. In Sec. VIII, a series of lower-energy effective Hamiltonians are constructed. We finally give a summary in Sec. IX.

II. LUTTINGER-KOHN HAMILTONIAN

In this paper, we adopt the 4×4 Luttinger-Kohn Hamiltonian [5, 14] to describe the hole kinetic energy in the Ge nanowire. The 4×4 Luttinger-Kohn Hamiltonian is accurate enough because the typical quantization energy (about tens of meV [37]) in the nanowire is much less than the spin-orbit energy gap (about 297 meV [60]). Thus, it is reasonable to neglect the effects of the spin-orbit split-off band. When we choose the wave vectors along the cubic axes of the crystal, i.e., $k_x \parallel [100]$, $k_y \parallel [010]$, and $k_z \parallel [001]$, the Luttinger-Kohn Hamiltonian reads [5, 14]

$$H_{\text{LK}} = \frac{\hbar^2}{2m_0} \left[\left(\gamma_1 + \frac{5\gamma_2}{2} \right) \mathbf{k}^2 - 2\gamma_2 (k_x^2 J_x^2 + k_y^2 J_y^2 + k_z^2 J_z^2) - 4\gamma_3 (\{k_x, k_y\} \{J_x, J_y\} + \text{c.p.}) \right], \quad (1)$$

where m_0 is the free electron mass, $\gamma_1 = 13.35$, $\gamma_2 = 4.25$ and $\gamma_3 = 5.69$ are Luttinger parameters of semiconductor Ge [61], $J_{x,y,z}$ are standard spin-3/2 matrices (for details see appendix A), c.p. denotes cyclic permutations, and $\{A, B\} = (AB + BA)/2$.

If the wave vectors $k_{x,y,z}$ are not along the three crystal cubic axes, we need to obtain the corresponding Luttinger-Kohn Hamiltonian using coordinate transformation [43, 62]. The calculations of the subband dispersions in a quasi-one-dimensional nanowire are indeed complicated, some studies even use pure numerical methods [63–67], the primitive Luttinger-Kohn Hamiltonian (1) is rarely used in theoretical studies. As such,

two types of approximations are usually made to the Luttinger-Kohn Hamiltonian (1).

The simplest and the most frequently used approximation is the spherical approximation [68, 69]. Simply replacing $\gamma_{2,3}$ with γ_s in Eq. (1), one obtains the Luttinger-Kohn Hamiltonian in the spherical approximation

$$H_{\text{LK}}^{\text{sp}} = \frac{\hbar^2}{2m_0} \left[\left(\gamma_1 + \frac{5}{2}\gamma_s \right) \mathbf{k}^2 - 2\gamma_s (\mathbf{k} \cdot \mathbf{J})^2 \right]. \quad (2)$$

The spherical approximation brings out a new Luttinger parameter γ_s . In most applications, the new parameter γ_s is set to $\gamma_s = (2\gamma_2 + 3\gamma_3)/5$ [37, 68]. Note that in the spherical Luttinger-Kohn Hamiltonian (2), the wave vectors $k_{x,y,z}$ are not necessary along particular crystal directions, as long as they are mutually perpendicular to each other. Hence, the spherical approximation is unable to reflect the dispersion anisotropy.

The other approximation is called the axial approximation [35, 36], which is regarded as a more advanced approximation in comparison with the spherical approximation. The axial approximation can describe the dispersion anisotropy to some extent through its directional dependent Luttinger parameters. The Luttinger-Kohn Hamiltonian in the axial approximation reads [2]

$$H_{\text{LK}}^{\text{ax}} = \frac{\hbar^2}{2m_0} \left[\gamma_1 \mathbf{k}^2 + \tilde{\gamma}_1 (k_x^2 + k_y^2 - 2k_z^2) \left(J_z^2 - \frac{5}{4} \right) - 2\tilde{\gamma}_2 (\{k_z, k_+\} \{J_z, J_-\} + \{k_z, k_-\} \{J_z, J_+\}) - \frac{\tilde{\gamma}_3}{2} (k_+^2 J_-^2 + k_-^2 J_+^2) \right], \quad (3)$$

where $k_{\pm} = k_x \pm ik_y$, $J_{\pm} = J_x \pm iJ_y$, and $\tilde{\gamma}_{1,2,3}$ are Luttinger parameters depending on the orientations of the coordinate axes $k_{x,y,z}$ in the crystal. The relationship between $\tilde{\gamma}$ and γ reads [2]

$$\begin{aligned} \tilde{\gamma}_1 &= (1 - \zeta)\gamma_2 + \zeta\gamma_3, \\ \tilde{\gamma}_2 &= 2\zeta\gamma_2/3 + (1 - 2\zeta/3)\gamma_3, \\ \tilde{\gamma}_3 &= (3 - \zeta)\gamma_2/6 + (3 + \zeta)\gamma_3/6, \end{aligned} \quad (4)$$

where $\zeta = \sin^2 \theta [3 - (3/8)(7 + \cos 4\phi) \sin^2 \theta]$, with θ being the azimuthal angle and ϕ being the polar angle of the k_z axis with respect to the [001] direction (see Fig. 1) [2].

Both the spherical (2) and the axial (3) Luttinger-Kohn Hamiltonians have very good symmetries. Hamiltonian $H_{\text{LK}}^{\text{sp}}$ commutes with both \mathbf{F}^2 and F_z [32], where $\mathbf{F} = \mathbf{L} + \mathbf{J}$ is the total angular momentum, with \mathbf{L} being the orbital angular momentum. Hamiltonian $H_{\text{LK}}^{\text{ax}}$ commutes with F_z only [2]. The conservation of F_z leads to an exact solution of the subband dispersions when either $H_{\text{LK}}^{\text{sp}}$ or $H_{\text{LK}}^{\text{ax}}$ is used [32–34]. Also, the axial approximation is most accurate for high-symmetry nanowire growth directions [001] ($\theta = \phi = 0$) and [111] ($\theta = \arccos(1/\sqrt{3})$, $\phi = \pi/4$) [2]. The contribution from the non-axial term in the primitive Luttinger-Kohn Hamiltonian for these two directions is almost negligible [34].

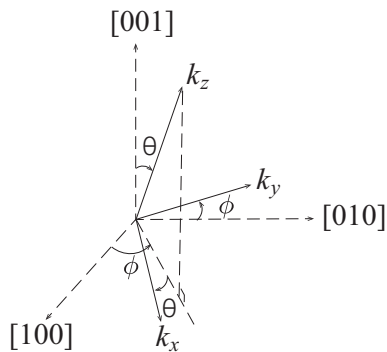


FIG. 1. The orientations of the coordinate axes $k_{x,y,z}$ relative to the crystal cubic axes are described by two angles θ and ϕ . Note that the k_y axis is in the $[100]$ - $[010]$ plane.

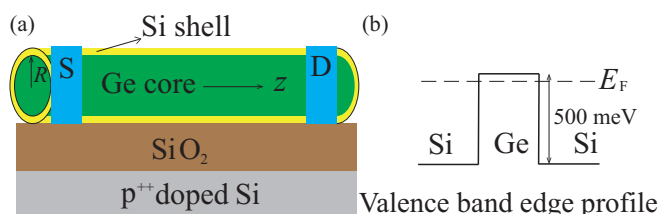


FIG. 2. (a) The setup used to achieve quasi-one-dimensional hole gas. The p^{++} doped Si substrate is covered with SiO_2 , on which a Ge/Si core/shell nanowire is deposited. The contacts between the nanowire and the source/drain electrodes are ohmic. (b) The valence band edge profile of the Ge/Si core/shell heterostructures. The dashed line indicates the position of the Fermi level.

III. EFFECTIVE MASS HAMILTONIAN AND THE ASSOCIATED SYMMETRIES

Quasi-one-dimensional hole gas is experimentally achievable in Ge/Si core/shell nanowire heterostructures [28, 70], Ge hut wire [29, 71, 72] etc. A typical experimental setup is shown in Fig. 2(a). The undoped Ge core can be populated with holes from the ohmic contacts when negative voltage is applied to the p^{++} doped Si substrate [30, 73]. The Si shell serves as a strong confinement to the hole gas due to the large valence band offset between Ge and Si (about 500 meV [74], see also Fig. 2(b)). Since the quantization energies of interest (about tens of meV [37]) are much less than this band offset, in the following the transverse confinement of the hole gas is treated as a hard wall.

We consider a cylindrical Ge nanowire, and its axis is defined as the z axis (see Fig. 2(a)). Certainly, the nanowire axis, i.e., the nanowire growth direction, can point along various crystal directions (see Fig. 1). The effective mass Hamiltonian of the hole gas reads

$$H_0 = H_{\text{LK}}^{\text{sp/ax}}(\mathbf{k} \rightarrow -i\nabla) + V(r), \quad (5)$$

where

$$V(r) = \begin{cases} 0, & r < R, \\ \infty, & r > R, \end{cases} \quad (6)$$

with R being the radius of the Ge core. Here we have chosen to study in a cylindrical coordinate system, where $r = \sqrt{x^2 + y^2}$, $\varphi = \arctan(y/x)$, and $z = z$. Also, this paper mainly focuses on the analytical or the exact solution to the effective mass Hamiltonian (5), such that we have employed either the spherical or the axial Luttinger-Kohn Hamiltonian.

Let us analyze the symmetries of the model (5) and their consequences. The symmetries of a model not only greatly help to simplify the corresponding calculations, but also give an intuitional explanation on the spin degeneracy in the subband dispersions [38]. First, because k_z is a conserved quantity in Hamiltonian (5), the energy eigenvalues must be written as a one-dimensional dispersion form $E(k_z)$.

Second, as we have mentioned in Sec. II, the z -component of the total angular momentum $F_z = -i\partial_\varphi + J_z$ is also a conserved quantity, such that Hamiltonian (5) can be diagonalized in the Hilbert subspace with a fixed F_z . The eigenfunction $\Psi(r, \varphi, z)$ in the Hilbert subspace specified with a general value of $F_z = m + 1/2$ ($m = 0, \pm 1, \pm 2 \dots$) can be written as [34, 38]

$$\Psi_{k_z, F_z}(r, \varphi, z) = \begin{pmatrix} \Psi_1(r)e^{i(m-1)\varphi} \\ \Psi_2(r)e^{im\varphi} \\ \Psi_3(r)e^{i(m+1)\varphi} \\ \Psi_4(r)e^{i(m+2)\varphi} \end{pmatrix} e^{ik_z z}, \quad (7)$$

where $\Psi_{1,2,3,4}(r)$ are the four components of the eigenfunction. Note that they are functions of the coordinate r only.

Third, Hamiltonian (5) is time-reversal invariant. The time-reversal operator for a spin-3/2 system reads

$$T = \Gamma_1 \Gamma_3 K, \quad (8)$$

where K is the usual complex conjugate operator, and $\Gamma_{1,3}$ are two 4×4 matrices given in appendix A [75]. One can easily verify the following relations $T^2 = -1$, $T\mathbf{J}T^{-1} = -\mathbf{J}$, and $T\mathbf{k}T^{-1} = -\mathbf{k}$, such that the time-reversal symmetry $TH_0T^{-1} = H_0$ becomes evident. Acting the time-reversal operator T on the eigenfunction (7), we have

$$\Psi_{-k_z, -F_z}(r, \varphi, z) = \begin{pmatrix} -\Psi_4^*(r)e^{-i(m+2)\varphi} \\ \Psi_3^*(r)e^{-i(m+1)\varphi} \\ -\Psi_2^*(r)e^{-im\varphi} \\ \Psi_1^*(r)e^{-i(m-1)\varphi} \end{pmatrix} e^{-ik_z z}. \quad (9)$$

At this stage, the Kramer's degeneracy only gives rise to $E(k_z, F_z) = E(-k_z, -F_z)$ [76].

Fourth, we introduce a spin-rotation operator $e^{i\theta J_z}$. Applying a unitary transformation of π rotation to Hamiltonian (5), we have $e^{i\pi J_z} H_0(k_z) e^{-i\pi J_z} = H_0(-k_z)$. Note that the eigenvalue of an operator is

unchanged during a unitary transformation. Replacing k_z with $-k_z$ in the last exponential factor in Eq. (9), we obtain an eigenfunction of $H_0(-k_z)$ (with the same eigenvalue as eigenfunction (9))

$$\begin{pmatrix} -\Psi_4^*(r)e^{-i(m+2)\varphi} \\ \Psi_3^*(r)e^{-i(m+1)\varphi} \\ -\Psi_2^*(r)e^{-im\varphi} \\ \Psi_1^*(r)e^{-i(m-1)\varphi} \end{pmatrix} e^{ik_z z}. \quad (10)$$

Applying an inverse unitary transformation of π rotation to this eigenfunction, i.e., acting the operator $e^{-i\pi J_z}$ on this eigenfunction, we have the other eigenfunction of $H_0(k_z)$

$$\Psi_{k_z, -F_z}(r, \varphi, z) = \begin{pmatrix} \Psi_4^*(r)e^{-i(m+2)\varphi} \\ \Psi_3^*(r)e^{-i(m+1)\varphi} \\ \Psi_2^*(r)e^{-im\varphi} \\ \Psi_1^*(r)e^{-i(m-1)\varphi} \end{pmatrix} e^{ik_z z}. \quad (11)$$

Via setting $-k_z$ to k_z in Eq. (9), one can also obtain Eq. (11). The cost in this way is that we must know the detailed k_z dependence of the components $\Psi_{1,2,3,4}(r)$ in advance.

Since both $\Psi_{k_z, F_z}(r, \varphi, z)$ and $\Psi_{k_z, -F_z}(r, \varphi, z)$ correspond to the same energy eigenvalue, while they must represent two distinct quantum states, i.e., the F_z values are different in these two states, we thus have the spin degeneracy in the hole subband dispersions

$$E(k_z, F_z) = E(k_z, -F_z). \quad (12)$$

Here, the two quantized directions of the hole spin are indicated by the ' \pm ' signs before F_z .

IV. BULK SOLUTIONS IN THE CYLINDRICAL COORDINATE SYSTEM

The potential $V(r)$ in Hamiltonian (5) is a hard-wall potential, it is zero inside the wall and infinity outside the wall. In this sense, the method of solving the model (5) should be similar to that of solving an infinite square-well in a quantum mechanics textbook [77], or more precisely to that of solving a hard-wall quantum dot with spin-orbit coupling [78, 79]. The procedure of solution can be summarized as follows. We first obtain both the bulk spectrum and the corresponding bulk wavefunctions governed by $H_{\text{LK}}^{\text{sp/ax}}$. We then write the eigenfunction of Hamiltonian (5) as a linear combination of the bulk wavefunctions. We finally let the eigenfunction vanish at the boundary $r = R$, such that a series of transcendental equations determining the subband energies are obtainable.

Due to the conservation of the total angular momentum F_z , the total Hilbert space of the bulk Hamiltonian $H_{\text{LK}}^{\text{sp/ax}}$ can be divided into a series of subspaces [32, 34]. The Hilbert subspace specified with a general value of the total angular momentum $F_z = m + 1/2$ is

spanned by $J_{m-1}(\mu r)e^{i(m-1)\varphi}|3/2\rangle$, $J_m(\mu r)e^{im\varphi}|1/2\rangle$, $J_{m+1}(\mu r)e^{i(m+1)\varphi}|-1/2\rangle$, and $J_{m+2}(\mu r)e^{i(m+2)\varphi}|-3/2\rangle$, where $J_m(\mu r)$ is the m -order Bessel function of the first kind [80]. We now seek the bulk spectrum and the corresponding bulk wavefunctions in this Hilbert subspace.

Before the detailed derivations, we first give some useful relations concerning the actions of the operators k_{\pm} and J_{\pm} on the Bessel functions and the spin-3/2 quantum states, respectively. The operators k_{\pm} are somewhat like the ladder operators on the quantum number m

$$\begin{aligned} k_+ J_m(\mu r)e^{im\varphi} &= i\mu J_{m+1}(\mu r)e^{i(m+1)\varphi}, \\ k_- J_m(\mu r)e^{im\varphi} &= -i\mu J_{m-1}(\mu r)e^{i(m-1)\varphi}, \end{aligned} \quad (13)$$

and operators J_{\pm} are the usual ladder operators on the spin-3/2 quantum number [77]

$$\begin{aligned} J_+ |M\rangle &= [(3/2 - M)(3/2 + M + 1)]^{1/2} |M + 1\rangle, \\ J_- |M\rangle &= [(3/2 + M)(3/2 - M + 1)]^{1/2} |M - 1\rangle, \end{aligned} \quad (14)$$

where $M = \pm 3/2, \pm 1/2$. Combining Eqs. (13) and (14), one easily finds the following operators, $k_+ J_-$, $k_- J_+$, $k_+^2 J_-^2$, and $k_-^2 J_+^2$, conserve the value of F_z . This result actually reflects the conservation of F_z in both Hamiltonians (2) and (3).

After some tedious derivations incorporating the two relations (13) and (14), and together with $(k_x^2 + k_y^2)J_m(\mu r)e^{im\varphi} = \mu^2 J_m(\mu r)e^{im\varphi}$, the bulk Hamiltonian $H_{\text{LK}}^{\text{ax}}$ can be written as a 4×4 matrix in the above Hilbert subspace [in unit of $\hbar^2/(2m_0)$] [34]

$$H_{\text{LK}}^{\text{ax}} = \begin{pmatrix} H_{11} & 2\sqrt{3}i\tilde{\gamma}_2 k_z \mu & \sqrt{3}\tilde{\gamma}_3 \mu^2 & 0 \\ h.c. & H_{22} & 0 & \sqrt{3}\tilde{\gamma}_3 \mu^2 \\ h.c. & 0 & H_{33} & -2\sqrt{3}i\tilde{\gamma}_2 k_z \mu \\ 0 & h.c. & h.c. & H_{44} \end{pmatrix}, \quad (15)$$

where $H_{11} = H_{44} = (\gamma_1 + \tilde{\gamma}_1)\mu^2 + (\gamma_1 - 2\tilde{\gamma}_1)k_z^2$, $H_{22} = H_{33} = (\gamma_1 - \tilde{\gamma}_1)\mu^2 + (\gamma_1 + 2\tilde{\gamma}_1)k_z^2$, and $h.c.$ stands for Hermitian conjugation ensuring the Hermiticity of $H_{\text{LK}}^{\text{ax}}$. If we want to use the spherical Luttinger-Kohn Hamiltonian, we just need to replace $\tilde{\gamma}_{1,2,3}$ with γ_s in Eq. (15) [32]. We also emphasize that this replacement is always feasible in the rest of the paper for obtaining the spherical approximation results. Diagonalizing the matrix (15), we obtain two branches of bulk spectrum

$$E_{\pm}^{\text{R}} = \frac{\hbar^2}{2m_0} [\gamma_1(\mu^2 + k_z^2) \pm \chi_{\mu}], \quad (16)$$

where $\chi_{\mu} = \sqrt{\tilde{\gamma}_1^2(\mu^2 - 2k_z^2)^2 + 3\mu^2(4\tilde{\gamma}_2^2 k_z^2 + \tilde{\gamma}_3^2 \mu^2)}$. For each branch of the bulk spectrum, there exist two bulk wavefunctions [34], i.e.,

$$\Psi_{\text{b1}}^{\pm}(r, \varphi) = \begin{pmatrix} \frac{2i\tilde{\gamma}_2 k_z}{\tilde{\gamma}_3 \mu} J_{m-1}(\mu r)e^{i(m-1)\varphi} \\ \frac{-\tilde{\gamma}_1(\mu^2 - 2k_z^2) \pm \chi_{\mu}}{\sqrt{3}\tilde{\gamma}_3 \mu^2} J_m(\mu r)e^{im\varphi} \\ 0 \\ J_{m+2}(\mu r)e^{i(m+2)\varphi} \end{pmatrix}, \quad (17)$$

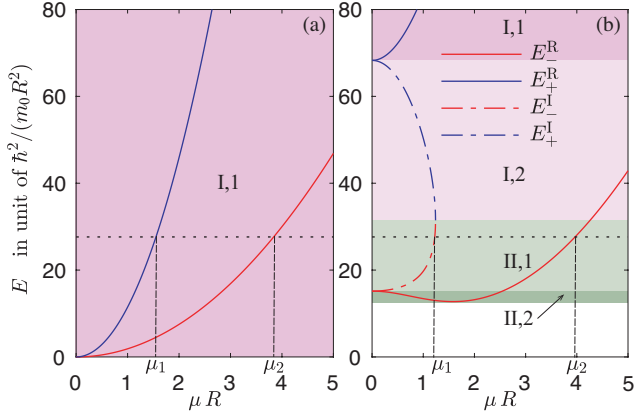


FIG. 3. The bulk hole dispersions for growth direction [001] with the longitudinal wave vector fixed at $k_z R = 0$ (a) and $k_z R = 2.5$ (b). We can specify the whole energy region as region I when $k_z R = 0$ or divide it into two regions I and II when $k_z R \neq 0$. A constant energy line in energy region I intersects the plus branch dispersion (either E_+^R or E_+^I) at μ_1 , and intersects the minus branch dispersion E_-^R at μ_2 . While a constant energy line in energy region II intersects the minus branch dispersion (either E_-^R or E_-^I) both at μ_1 and μ_2 . Reprinted figure from [34].

and

$$\Psi_{b2}^{\pm}(r, \varphi) = \begin{pmatrix} \frac{\tilde{\gamma}_1(\mu^2 - 2k_z^2) \pm \chi_{\mu}}{\sqrt{3}\tilde{\gamma}_3\mu^2} J_{m-1}(\mu r) e^{i(m-1)\varphi} \\ -\frac{2i\tilde{\gamma}_2 k_z}{\tilde{\gamma}_3\mu} J_m(\mu r) e^{im\varphi} \\ J_{m+1}(\mu r) e^{i(m+1)\varphi} \\ 0 \end{pmatrix}. \quad (18)$$

These bulk wavefunctions are very important in obtaining both the eigenvalues and the corresponding eigenfunctions of Hamiltonian (5).

We now analyze the bulk dispersions obtained in Eq. (16), where μ is presumed to be real. When $k_z = 0$, the E_+^R branch and the E_-^R branch touch with each other at the dispersion minimum (see Fig. 3(a)). A constant energy line always intersects the E_{\pm}^R dispersions two times. While when $k_z \neq 0$, the E_+^R branch lies above the E_-^R branch, and leaves a finite gap region, i.e., the I,2 and II,1 subregions in Fig. 3(b). A constant energy line in the gap region intersects the E_{\pm}^R dispersions only one time. This result indicates that Bessel functions with real argument μr are inadequate to give rise to the complete bulk dispersions. We also need to consider Bessel functions $J_m(i\mu r)$ with imaginary argument $i\mu r$. A simple replacement of μ with $i\mu$ in Eq. (16) gives us the bulk dispersions in terms of Bessel functions with imaginary argument

$$E_{\pm}^I = E_{\pm}^R|_{\mu=i\mu}. \quad (19)$$

The above two bulk dispersions are shown by the dashed-dot lines in Fig. 3. Now a constant energy line in the whole energy region always intersects the bulk dispersions two times. Moreover, we can specify the whole

energy region as region I when $k_z R = 0$ or divide it into two regions I and II when $k_z R \neq 0$ (see Fig. 3). Note that the results in Fig. (3) are for growth direction [001], the results for other growth directions, such as [111] and [110], are similarly obtainable.

V. THE TRANSCENDENTAL EQUATIONS

The eigenfunction (7) can be written as a linear combination of the four bulk wave functions shown in Eqs. (17) and (18). In doing so, we should carefully take into account of the division of the energy region shown in Fig. 3. In energy region I, we should choose two from the '+' branch and two from the '-' branch, because a given energy line in this region always intersects the '+' branch one time and the '-' branch one time (see Fig. 3(a)). While in energy region II, all the four bulk wave functions should be chosen from the '-' branch, a given energy line in this region always intersects the '-' branch two times (see Fig. 3(b)). Therefore, the four components of the eigenfunction in the corresponding energy region I/II ($\rightarrow \pm$) can be written as [34]

$$\begin{aligned} \Psi_1(r) &= \left(c_1 \frac{2i\tilde{\gamma}_2 k_z}{\tilde{\gamma}_3\mu_1} + c_2 \frac{\tilde{\gamma}_1(\mu_1^2 - 2k_z^2) \pm \chi_{\mu_1}}{\sqrt{3}\tilde{\gamma}_3\mu_1^2} \right) J_{m-1}(\mu_1 r) \\ &\quad + \left(c_3 \frac{2i\tilde{\gamma}_2 k_z}{\tilde{\gamma}_3\mu_2} + c_4 \frac{\tilde{\gamma}_1(\mu_2^2 - 2k_z^2) - \chi_{\mu_2}}{\sqrt{3}\tilde{\gamma}_3\mu_2^2} \right) J_{m-1}(\mu_2 r), \\ \Psi_2(r) &= \left(c_1 \frac{-\tilde{\gamma}_1(\mu_1^2 - 2k_z^2) \pm \chi_{\mu_1} - c_2 \frac{2i\tilde{\gamma}_2 k_z}{\tilde{\gamma}_3\mu_1}}{\sqrt{3}\tilde{\gamma}_3\mu_1^2} \right) J_m(\mu_1 r) \\ &\quad + \left(c_3 \frac{-\tilde{\gamma}_1(\mu_2^2 - 2k_z^2) - \chi_{\mu_2} - c_4 \frac{2i\tilde{\gamma}_2 k_z}{\tilde{\gamma}_3\mu_2}}{\sqrt{3}\tilde{\gamma}_3\mu_2^2} \right) J_m(\mu_2 r), \\ \Psi_3(r) &= c_2 J_{m+1}(\mu_1 r) + c_4 J_{m+1}(\mu_2 r), \\ \Psi_4(r) &= c_1 J_{m+2}(\mu_1 r) + c_3 J_{m+2}(\mu_2 r), \end{aligned} \quad (20)$$

where $c_{1,2,3,4}$ are the expansion coefficients to be determined, and

$$\mu_{1,2} = \left(\frac{-b \mp \sqrt{b^2 - 4ac}}{2a} \right)^{1/2}, \quad (21)$$

with

$$\begin{aligned} a &= \gamma_1^2 - \tilde{\gamma}_1^2 - 3\tilde{\gamma}_3^2, \\ b &= 2[\gamma_1^2 k_z^2 + 2(\tilde{\gamma}_1^2 - 3\tilde{\gamma}_2^2)k_z^2 - 2\gamma_1 m_0 E/\hbar^2], \\ c &= \gamma_1^2 k_z^4 - 4\tilde{\gamma}_1^2 k_z^4 - 4\gamma_1 k_z^2 m_0 E/\hbar^2 + 4m_0^2 E^2/\hbar^4 \quad (22) \end{aligned}$$

Here $\mu_{1,2}$ are obtained by inversely solving Eq. (16). Note that μ_2 is always real in the whole energy region (see Fig. 3), while μ_1 can be real in the energy subregions I,1 and II,2 or imaginary in the energy subregions I,2 and II,1 [see Fig. 3(b)].

Imposing the hard-wall boundary condition to the eigenfunction, i.e., $\Psi(R, \varphi, z) = 0$, we obtain four equations on the expansion coefficients $c_{1,2,3,4}$ (for details see appendix B). The determinant of the coefficient matrix must be zero, such that we have the following transcendental equations [34]

$$\begin{vmatrix} \frac{2i\tilde{\gamma}_2 k_z}{\tilde{\gamma}_3 \mu_1} J_{m-1}(\mu_1 R) & \frac{\tilde{\gamma}_1(\mu_1^2 - 2k_z^2) \pm \chi_{\mu_1}}{\sqrt{3}\tilde{\gamma}_3 \mu_1^2} J_{m-1}(\mu_1 R) & \frac{2i\tilde{\gamma}_2 k_z}{\tilde{\gamma}_3 \mu_2} J_{m-1}(\mu_2 R) & \frac{\tilde{\gamma}_1(\mu_2^2 - 2k_z^2) - \chi_{\mu_2}}{\sqrt{3}\tilde{\gamma}_3 \mu_2^2} J_{m-1}(\mu_2 R) \\ -\frac{\tilde{\gamma}_1(\mu_1^2 - 2k_z^2) \pm \chi_{\mu_1}}{\sqrt{3}\tilde{\gamma}_3 \mu_1^2} J_m(\mu_1 R) & -\frac{2i\tilde{\gamma}_2 k_z}{\tilde{\gamma}_3 \mu_1} J_m(\mu_1 R) & -\frac{\tilde{\gamma}_1(\mu_2^2 - 2k_z^2) - \chi_{\mu_2}}{\sqrt{3}\tilde{\gamma}_3 \mu_2^2} J_m(\mu_2 R) & -\frac{2i\tilde{\gamma}_2 k_z}{\tilde{\gamma}_3 \mu_2} J_m(\mu_2 R) \\ 0 & J_{m+1}(\mu_1 R) & 0 & J_{m+1}(\mu_2 R) \\ J_{m+2}(\mu_1 R) & 0 & J_{m+2}(\mu_2 R) & 0 \end{vmatrix} = 0. \quad (23)$$

Note that the ‘ \pm ’ signs respectively give rise to the transcendental equation in the energy regions I/II. The energy eigenvalue E is the only unknown in Eq. (23). We can obtain the hole subband dispersions $E(k_z)$ via numerically solving Eq. (23). Once an eigenvalue E is obtained, we can solve the coefficients $c_{1,2,3,4}$ from the matrix equation (see appendix B), such that the eigenfunction corresponding to E is also known [38].

We discuss here both the energy eigenvalues and the corresponding eigenfunctions at the special wave vector site $k_z = 0$. They are important in constructing the low-energy effective Hamiltonian of the hole gas (see Sec. VIII). Also, several studies have studied the hole g -factor at this site by using the spherical approximation [81–83]. When $k_z = 0$, only energy region I exists [see Fig. 3(a)], and the plus sign ‘+’ transcendental equation (23) can be reduced to two independent equations, one reads [34]

$$\begin{aligned} & \frac{\sqrt{\tilde{\gamma}_1^2 + 3\tilde{\gamma}_3^2} + \tilde{\gamma}_1}{\sqrt{\tilde{\gamma}_1^2 + 3\tilde{\gamma}_3^2} - \tilde{\gamma}_1} J_{m-1}(\mu_1 R) J_{m+1}(\mu_2 R) \\ & + J_{m-1}(\mu_2 R) J_{m+1}(\mu_1 R) = 0, \end{aligned} \quad (24)$$

and the other reads [34]

$$\begin{aligned} & \frac{\sqrt{\tilde{\gamma}_1^2 + 3\tilde{\gamma}_3^2} + \tilde{\gamma}_1}{\sqrt{\tilde{\gamma}_1^2 + 3\tilde{\gamma}_3^2} - \tilde{\gamma}_1} J_m(\mu_2 R) J_{m+2}(\mu_1 R) \\ & + J_m(\mu_1 R) J_{m+2}(\mu_2 R) = 0. \end{aligned} \quad (25)$$

The success of this reduction can be traced back to the fact that the bulk Hamiltonian $H_{\text{LK}}^{\text{ax}}$ is block diagonalized at $k_z = 0$ (see Eq. (15)). If the energy eigenvalue E is solved from Eq. (24), we find a simple solution of the expansion coefficients

$$c_2 = iJ_{m+1}(\mu_2 R), \quad c_4 = -iJ_{m+1}(\mu_1 R), \quad c_1 = c_3 = 0. \quad (26)$$

This result indicates that two components of the eigenfunction [see Eq. (20)] are zero, i.e., $\Psi_2(r) = \Psi_4(r) = 0$. If the energy eigenvalue E is solved from Eq. (25), the expansion coefficients can be solved as

$$c_1 = J_{m+2}(\mu_2 R), \quad c_3 = -J_{m+2}(\mu_1 R), \quad c_2 = c_4 = 0. \quad (27)$$

This result indicates that the following two components $\Psi_1(r)$ and $\Psi_3(r)$ of the eigenfunction are zero instead.

Hence, at the site $k_z = 0$, the eigenfunctions always have two vanishing components, i.e., either $\Psi_{1,3}(r)$ or $\Psi_{2,4}(r)$ are zero [37, 38, 83]. We also note that by choosing the simple coefficient solutions as Eqs. (26) and (27), the eigenfunctions are not normalized.

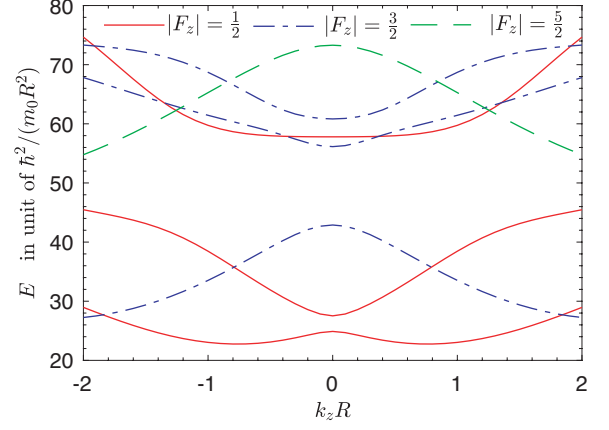


FIG. 4. Hole subband dispersions for growth direction [001]. For a moderate nanowire radius $R = 10$ nm, the energy unit is $\hbar^2/(m_0 R^2) \approx 0.763$ meV. The energy gap at the anticrossing $k_z R = 0$ of the lowest two subband dispersions is about $2.63\hbar^2/(m_0 R^2)$. The band minima are located at $k_z R \approx \pm 0.76$. Each dispersion line is two-fold (spin) degenerate. Reprinted figure from [34].

Here we emphasize again, the results based on the spherical Luttinger-Kohn Hamiltonian are obtainable via simply replacing $\tilde{\gamma}_{1,2,3}$ with γ_s in equations from (20) to (27). The result of Sercel and Vahala [32, 84] is nicely recovered in this case.

VI. SUBBAND DISPERSIONS

A. Growth direction [001]

When the growth direction of the Ge nanowire is along the [001] crystal axis, i.e., $k_x \parallel [100]$, $k_y \parallel [010]$, and $k_z \parallel [001]$, we have $\tilde{\gamma}_1 = \gamma_2$, $\tilde{\gamma}_2 = \gamma_3$, and $\tilde{\gamma}_3 = (\gamma_2 + \gamma_3)/2$ by setting $\theta = \phi = 0$ in Eq. (4) [85]. Solving Eq. (23) using these values of $\tilde{\gamma}_{1,2,3}$, we have the hole subband dispersions for growth direction [001] (see Fig. 4). Each line in the figure is two-fold (spin) degenerate. The lowest two subband dispersions can be regarded as two shifted parabolic curves with an anticrossing at $k_z R = 0$. The energy gap at the anticrossing is about $2.63\hbar^2/(mR^2)$. The band minima are located at $k_z R \approx \pm 0.76$. The lowest three subband dispersions obtained here agree well with that obtained previously using perturbation method [41].

We now consider the effect of the non-axial term in the primitive Luttinger-Kohn Hamiltonian (1). The dif-

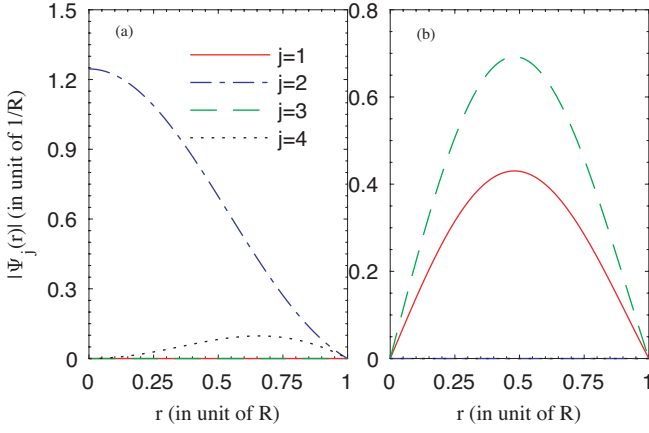


FIG. 5. The ground state (a) and the first excited state (b) wavefunctions at $k_z R = 0$ for growth direction [001]. The four components $\Psi_{1,2,3,4}(r)$ of the wavefunction (7) are plotted as a function of the coordinate r . Reprinted figure from [34].

ference between H_{LK} and H_{LK}^{ax} for growth direction [001] reads [2, 85]

$$H'_{001} = \frac{\hbar^2}{8m_0}(\gamma_3 - \gamma_2)(k_+^2 J_+^2 + k_-^2 J_-^2). \quad (28)$$

Using the perturbation theory, we find H'_{001} only has perturbation matrix elements between the eigenstates of $|F_z| = 1/2$ and $|F_z| \geq 7/2$ [34]. The lowest two subband dispersions shown in Fig. 4 are thus very accurate, because they are well separated from those $|F_z| \geq 7/2$ subband dispersions (even not shown in the figure because of their large energies).

The ground state and the first excited state wavefunctions at $k_z R = 0$ are shown in Figs. 5(a) and (b), respectively. As we have demonstrated in Sec. V, the wavefunctions at this site always have two vanishing components. Here, the ground state has components $\Psi_{2,4}(r) \neq 0$ (see Fig. 5(a)), while the first excited state has components $\Psi_{1,3}(r) \neq 0$ (see Fig. 5(b)).

B. Growth direction [111]

When the growth direction of the Ge nanowire is along the [111] crystal axis, i.e., $k_x \parallel [11\bar{2}]$, $k_y \parallel [\bar{1}10]$, and $k_z \parallel [111]$, we have $\tilde{\gamma}_1 = \gamma_3$, $\tilde{\gamma}_2 = (2\gamma_2 + \gamma_3)/3$, and $\tilde{\gamma}_3 = (\gamma_2 + 2\gamma_3)/3$ by setting $\theta = \arccos(1/\sqrt{3})$ and $\phi = \pi/4$ in Eq. (4) [86, 87]. Solving Eq. (23) using these $\tilde{\gamma}$ values, we have the hole subband dispersions for growth direction [111] (see Fig. 6). The energy gap at the anti-crossing of the lowest two subband dispersions is about $0.61\hbar^2/(mR^2)$, much smaller than that for growth direction [001]. The band minima are located at $k_z R \approx \pm 0.40$, much closer to the center of k_z space than that for growth direction [001].

The difference between H_{LK} and H_{LK}^{ax} for growth di-

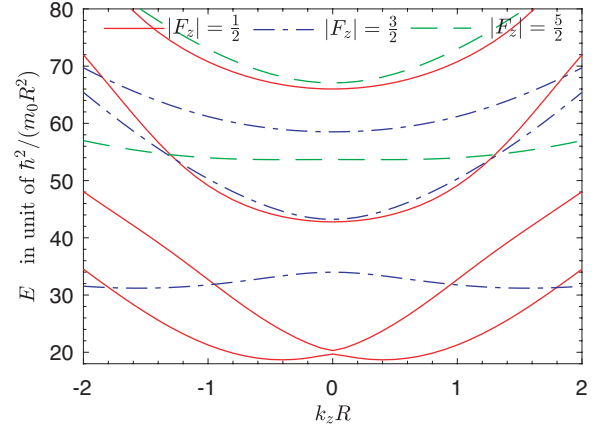


FIG. 6. Hole subband dispersions for growth direction [111]. The energy gap at the anticrossing $k_z R = 0$ of the lowest two subband dispersions is about $0.61\hbar^2/(m_0R^2)$. The band minima are located at $k_z R \approx \pm 0.4$. Each dispersion line is two-fold (spin) degenerate. Reprinted figure from [34].

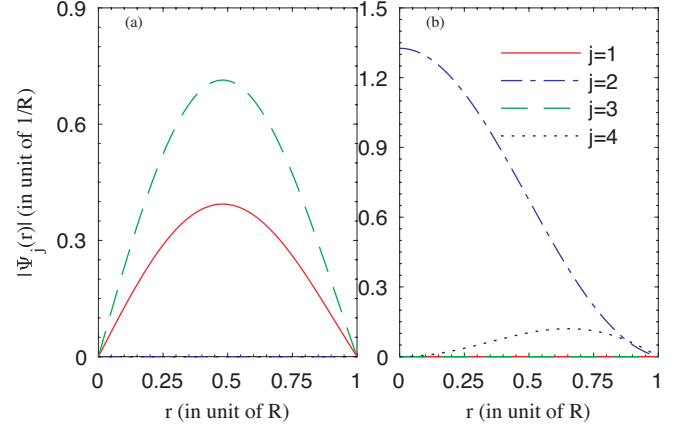


FIG. 7. The ground state (a) and the first excited state (b) wavefunctions at $k_z R = 0$ for growth direction [111]. The four components $\Psi_{1,2,3,4}(r)$ of the wavefunction (7) are plotted as a function of the coordinate r . Reprinted figure from [34].

rection [111] reads [86, 87]

$$H'_{111} = -\frac{(\gamma_3 - \gamma_2)\hbar^2}{3\sqrt{2}m_0} \left(k_+^2 \{J_z, J_+\} + k_-^2 \{J_z, J_-\} + k_z(k_+ J_+^2 + k_- J_-^2) \right). \quad (29)$$

Now we find H'_{111} only has perturbation matrix elements between eigenstates of $|F_z| = 1/2$ and $|F_z| \geq 5/2$ [34]. The lowest two subband dispersions shown in Fig. 4 are still accurate enough, because those $|F_z| \geq 5/2$ subband dispersions lies much higher.

The ground and the first excited state wavefunctions at $k_z R = 0$ are shown in Figs. 7(a) and (b), respectively. Comparing the wavefunctions here with that for growth direction [001], we find a quantum state inversion has occurred. For the growth direction [111], we have

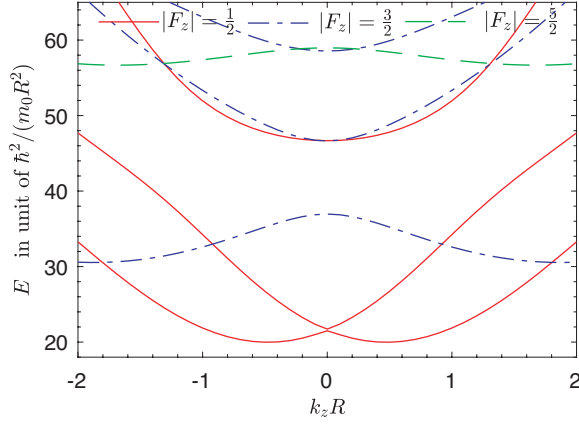


FIG. 8. Hole subband dispersions for growth direction [110]. The energy gap at the anticrossing $k_z R = 0$ of the lowest two subband dispersions is about $0.23\hbar^2/(m_0R^2)$. The band minima are located at $k_z R \approx \pm 0.5$. Each dispersion line is two-fold (spin) degenerate.

the ground state $\Psi_{1,3}(r) \neq 0$ and the first excited state $\Psi_{2,4}(r) \neq 0$ [see Fig. 7]. While for the growth direction [001], we have the ground state $\Psi_{2,4}(r) \neq 0$ and the first excited state $\Psi_{1,3}(r) \neq 0$ instead [see Fig. 5]. Quantum state inversion implies there is a potential gap closing site between growth directions [001] and [111] [34].

C. Growth direction [110]

When the growth direction of the Ge nanowire is along the [110] crystal axis, i.e., $k_x \parallel [00\bar{1}]$, $k_y \parallel [\bar{1}10]$, and $k_z \parallel [110]$, we have $\tilde{\gamma}_1 = (\gamma_2 + 3\gamma_3)/4$, $\tilde{\gamma}_2 = (\gamma_2 + \gamma_3)/2$, and $\tilde{\gamma}_3 = (3\gamma_2 + 5\gamma_3)/8$ by setting $\theta = \pi/2$ and $\phi = \pi/4$ in Eq. (4) [85]. The hole subband dispersions for growth direction [110] are shown in Fig. 8. The energy gap at the anticrossing of the lowest two subband dispersions is only about $0.23\hbar^2/(mR^2)$, even smaller than that for growth direction [111]. The band minima are located at $k_z R \approx \pm 0.50$.

The difference between H_{LK} and H_{LK}^{ax} for growth direction [110] is relatively complicated [2]

$$\begin{aligned}
 H'_{110} = & -\frac{3\hbar^2}{96m_0}(\gamma_3 - \gamma_2)\left(6(k_+^2 + k_-^2)(J_z^2 - 5/4) \right. \\
 & + 16k_z k_+ \{J_z, J_+\} + 16k_z k_- \{J_z, J_-\} \\
 & \left. - 2(k_+ k_- - 2k_z^2)(J_+^2 + J_-^2) - 3(k_+^2 J_+^2 + k_-^2 J_-^2)\right). \quad (30)
 \end{aligned}$$

Detailed calculations show H'_{110} has perturbation matrix elements between the eigenstates of $|F_z| = 1/2$ and $|F_z| \geq 3/2$. Hence, the axial approximation is less accurate for growth direction [110] than growth directions [100] and [111]. Also, the crossings between the dispersion lines of $|F_z| = 1/2$ and $|F_z| = 3/2$ in Fig. 8 will

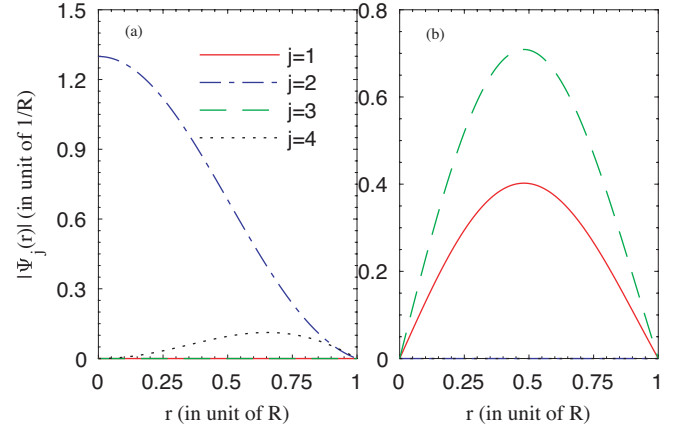


FIG. 9. The ground state (a) and the first excited state (b) wavefunctions at $k_z R = 0$ for growth direction [110]. The four components $\Psi_{1,2,3,4}(r)$ of the wavefunction (7) are plotted as a function of the coordinate r .

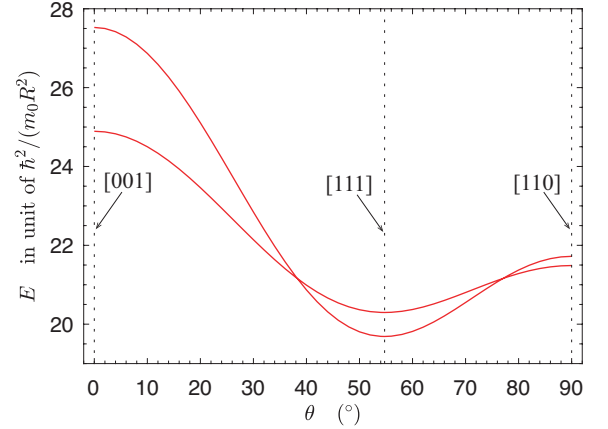


FIG. 10. The lowest two subband energies at $k_z R = 0$ as a function of the growth direction θ . Here ϕ is fixed at $\phi = 45^\circ$. The energy gap closes both at $\theta \approx 38.258^\circ$ and at $\theta \approx 77.069^\circ$.

become anticrossings when H'_{110} is taken into consideration [41].

The ground and the first excited state wavefunctions at $k_z R = 0$ are shown in Figs. 9(a) and (b), respectively. We find both growth directions [001] (see Fig. 5) and [110] (see Fig. 9) have normal ground and first excited states, while growth direction [111] (see Fig. 7) have inverted ground and first excited states. The ground state of growth directions [001] and [110] becomes the first excited state of growth direction [111].

Quantum state inversion has been extensively studied in topological insulator [88, 89], and state inversion usually indicates the existence of a gap closing site. We anticipate there are gap closing sites between growth directions [001]/[110] and [111]. When one angle of the growth direction is fixed at $\phi = 45^\circ$, and the other angle θ is varied from 0° to 90° , i.e., from growth direction [001] to [110], the lowest two subband energies at $k_z R = 0$ as

a function of θ are shown in Fig. 10. We indeed find two gap closing sites at $\theta \approx 38.258^\circ$ and $\theta \approx 77.069^\circ$.

VII. SPIN SPLITTING IN A STRONG MAGNETIC FIELD

The lowest two subband dispersions, i.e., the lowest two solid lines shown in Figs. 4, 6, and 8 can be regarded as two shifted parabolic curves with an anticrossing at $k_z R = 0$. Especially, the energy gap at the anticrossing is rather small for both growth directions [111] and [110]. This peculiar low-energy subband structure indicates the existence of a strong ‘spin’ (pseudo spin)-orbit coupling [40, 51], where the ‘spin’ is introduced to describe the two shifted directions of the parabolic curve. In order to make use of this strong ‘spin’-orbit coupling, we need to lift the spin degeneracy in the subband dispersions. This can be simply achieved by a strong magnetic field, such that two sets of combined dispersions with strong ‘spin’-orbit coupling and isolated from each other are obtainable [40].

The magnetic field can be applied either longitudinally or transversely. The magnetic field enters into the effective mass Hamiltonian via the vector potential [37, 90], the effective mass Hamiltonian now reads

$$H = H_{\text{LK}}^{\text{sp/ax}}(\mathbf{k} \rightarrow \mathbf{k}' = \mathbf{k} + e\mathbf{A}/\hbar) + V(r) + 2\kappa\mu_B\mathbf{B} \cdot \mathbf{J}, \quad (31)$$

where $\mathbf{A} = (-B_z y/2, B_z x/2, 0)$ when the field is longitudinal and $\mathbf{A} = (0, 0, B_x y)$ when the field is transverse, $\kappa = 3.41$ is the Luttinger magnetic parameter of semiconductor Ge [61]. We have properly chosen the vector potential such that k_z is still conserved in Hamiltonian (31). In the following, we use perturbation theory to calculate the spin splitting in the subband dispersions, and Hamiltonian (31) can be written as two parts

$$H = H_0 + H_B, \quad (32)$$

where H_0 is zeroth order term given by Eq. (5) and the perturbation term H_B contains both the Zeeman term and all the orbital terms of the magnetic field. The detailed form of H_B' is given in appendix C.

As we have shown in Sec. V, both the eigenvalues and the corresponding eigenstates of H_0 are exactly obtainable. Now, we calculate the magnetic field induced spin splitting in the lowest two subband dispersions. Because the energy gap at the anticrossing is rather small for both growth directions [111] and [110], here we must use quasi-degenerate perturbation theory, i.e., Hamiltonian (31) is written as a 4×4 matrix in the quasi degenerate Hilbert subspace spanned by lowest four eigenstates. The detailed calculation procedure for the case of the spherical approximation was given in Ref. [39]. Diagonalizing the 4×4 matrix, we obtain the subband dispersions with spin splitting.

In Figs. 11, 12, and 13, we show the spin splitting in the lowest two subband dispersions for growth directions

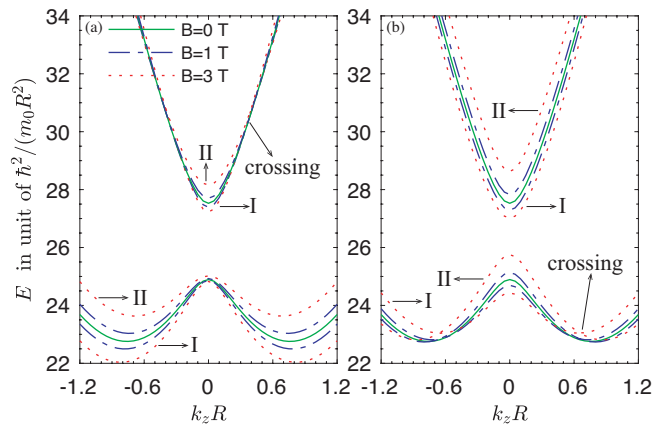


FIG. 11. Spin splitting in the lowest two subband dispersions for growth direction [001]. The results of the strong longitudinal field (a) and the strong transverse field (b).

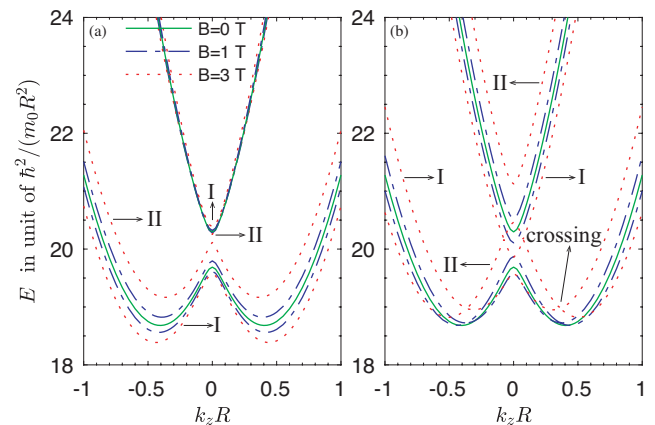


FIG. 12. Spin splitting in the lowest two subband dispersions for growth direction [111]. The results of the strong longitudinal field (a) and the strong transverse field (b).

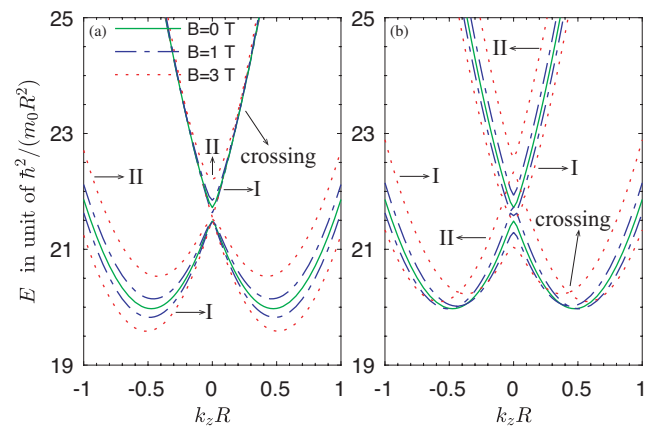


FIG. 13. Spin splitting in the lowest two subband dispersions for growth direction [110]. The results of the strong longitudinal field (a) and the strong transverse field (b).

[001], [111], and [110], respectively. Also, the results of the longitudinal field and the transverse field are shown in panel (a) and panel (b) of each figure, respectively. We can see subband crossings in Figs. 11, 12, and 13, and these crossings imply the possibility of classifying the subband dispersions into different spin sets, e.g., one set I belongs to spin down and the other set II belongs to spin up. Each set I or II can be modelled by a two-band Hamiltonian [40]

$$H^{\text{ef}} = \hbar^2 k_z^2 / (2m_h^*) + \alpha \sigma^x k_z + g_h^* \mu_B B \sigma^z / 2, \quad (33)$$

where $\sigma^{x,z}$ are Pauli ‘spin’ matrices. The ‘spin’-orbit coupling α and the effective g -factor g_h^* are magnetic field dependent [51]. This two-band description of each set is further confirmed in Sec. VIII via constructing the low-energy effective Hamiltonian of the hole gas.

We note that, in terms of the real hole spin, a similar Hamiltonian like Eq. (33) is also obtainable by using a strong electric field to lift the spin-degeneracy [37, 44, 55]. The difference between the ‘spin’ (pseudo spin) and real spin is obvious, the real spin splitting is the splitting between lines I and II in Figs. 11, 12, and 13. Also, the longitudinal g -factor of the real hole spin is rather small, about 0.14 [37, 59, 73] calculated using the spherical approximation. While the longitudinal g -factor of the hole ‘spin’ can be very large in the small magnetic field region [40, 51].

Quantum state inversion also leaves some trails in these figures. For example, when the magnetic field is longitudinal, for both [001] and [110] growth directions, the spin splitting at $k_z R = 0$ of the lowest subband dispersion is much smaller than that of the second lowest subband dispersion (see Figs. 11(a) and 13(a)), while this result becomes reversed for [111] growth direction (see Fig. 12(a)).

VIII. LOW-ENERGY EFFECTIVE HAMILTONIAN

We now construct the low-energy effective Hamiltonians that qualitatively describe both the lowest two subband dispersions (see Figs. 4, 6, and 8) and their spin splitting in a strong magnetic field (see Figs. 11, 12, and 13). We first focus on the absent magnetic field case, the low-energy effective Hamiltonian can be constructed as follows. The k_z terms in Hamiltonian H_0 (5) are treated as perturbation, e.g., we write $H_0 = H_0|_{k_z=0} + H_0|_{k_z \neq 0}$. The lowest four eigenstates of $H_0|_{k_z=0}$ are solved as $|e+\rangle$, $|e-\rangle$, $|g+\rangle$, and $|g-\rangle$ (see Figs. 5, 7, and 9). Then, H_0 can be written as an effective 4×4 Hamiltonian in the Hilbert subspace spanned by the above four eigenstates. In 2011, Kloeffel et al. obtained the following effective

Hamiltonian based on the spherical approximation [37]

$$H_0^{\text{ef}} = \frac{\hbar^2 k_z^2}{4} \left(\frac{1}{m_e^*} + \frac{1}{m_g^*} \right) + C \frac{\hbar^2}{m_0 R} k_z \tau^x s^x + \left[\frac{\hbar^2 k_z^2}{4} \left(\frac{1}{m_e^*} - \frac{1}{m_g^*} \right) + \frac{\Delta}{2} \frac{\hbar^2}{m_0 R^2} \right] \tau^z. \quad (34)$$

where $\boldsymbol{\tau}$ and \mathbf{s} are Pauli matrices defined in the orbital $\{g, e\}$ and spin $\{+, -\}$ subspaces, respectively, Δ is the energy spacing between $|e\pm\rangle$ and $|g\pm\rangle$. The values of the parameters $m_{e,g}^*$, C , and Δ are given in Tab. I, and their analytical formulas are given in appendix D.

The effective Hamiltonian (34) indeed qualitatively reproduces the two shifted parabolic curves shown in Figs. 4, 6, and 8. However, both the site and the magnitude of the subband minimum predicted by the effective Hamiltonian (34) are slightly different from the exact results given by Eq. (23) [40]. This discrepancy is due to the fact that H_0^{ef} is valid only at small $k_z R$ ($k_z R \ll 1$), while the exact site of the band minimum is located at $|k_z R| \approx 0.4 \rightarrow 0.76$ depending on the growth direction. We also give the band fitting values of $m_{e,g}^*$, C , and Δ in Tab. I [40]. The k_z^2 term in the second line of Eq. (34) is much smaller than that in the first line, we thus neglect this term in the following. Hence, we have

$$H_0^{\text{ef}} \approx \frac{\hbar^2 k_z^2}{2m_h^*} + C \frac{\hbar^2}{m_0 R} k_z \tau^x s^x + \frac{\Delta}{2} \frac{\hbar^2}{m_0 R^2} \tau^z, \quad (35)$$

where $1/m_h^* = (m_e^* + m_g^*) / (2m_e^* m_g^*)$. We also emphasize that the reduction from Eq. (34) to Eq. (35) is an approximation, and does not mean $m_e^* = m_g^*$.

Since the low-energy effective Hamiltonian governed by Hamiltonian H_0 is constructed successfully, we now move to construct the effective Hamiltonian of the magnetic term H_B that gives rise to the spin splitting in Figs. 11, 12, and 13. In the following, we consider separately the cases of the longitudinal field and the transverse field. In addition, the spin splitting induced by an external electric field is also considered briefly.

Note that if we want to keep the small k_z^2 term in the second line of Eq. (34), the classification of the subband dispersions into different spin sets is still feasible. We just need to add this term back to the Zeeman term in Eqs. (37), (38), (40), and (41) given in the following.

A. The strong longitudinal field case

When the magnetic field is applied longitudinally, i.e., the field $\mathbf{B} = (0, 0, B)$ is parallel to the nanowire axis, in the low-energy Hilbert subspace mentioned above, the magnetic term H_B in Eq. (32) can also be written as an effective 4×4 Hamiltonian [37, 40]

$$H_B^{\text{ef}} = \mu_B B (Z_1 s^z + Z_2 \tau^z s^z - Z_3 k_z R \tau^y s^y) + \frac{e^2 B^2 R^2}{2m_0} Z_4 \tau^z, \quad (36)$$

TABLE I. The parameters of the effective Hamiltonians. These values are calculated using the formulas given in appendix D, and those values given in the parentheses are obtained by a band fitting. The values based on the spherical and the axial approximations are indicated by ‘sp’ and [001], [111], and [110], respectively.

	m_z^*/m_0^a	m_g^*/m_0	C	Δ	Z_1	Z_2	Z_3	Z_4	X_1	X_2	X_3	X_4	U
sp	0.054 (0.074)	0.043 (0.074)	7.27 (7.12)	0.77	0.75	0.82	-2.38 (-3.62)	0.65	2.73	-0.18	8.04 (4.66)	0.57	0.15
[001]	0.058 (0.092)	0.046 (0.092)	8.83 (8.50)	2.63	0.82	1.23	-2.76 (-4.15)	0.65	3.22	0.32	7.51 (5.12)	0.47	0.16
[111]	0.051 (0.066)	0.041 (0.066)	6.28 (6.22)	-0.61	0.75	0.46	-2.16 (-3.34)	0.65	2.35	-0.42	8.23 (6.52)	0.67	0.15
[110]	0.053 (0.071)	0.042 (0.071)	6.89 (6.77)	0.23	0.74	0.69	-2.30 (-3.29)	0.65	2.59	-0.27	8.13 (6.20)	0.61	0.15

^a m_0 is the free electron mass

where Z_i ($i = 1, 2, 3, 4$) are parameters describing both the Zeeman and the orbital effects of the longitudinal field (see appendix D). Note that the Z_4 term is caused by orbital effects of the magnetic field proportional to B^2 , and cannot be neglected because here the magnetic field is strong. The values of $Z_{1,2,3,4}$ based on both the spherical and axial approximations are given in Tab. I. Interestingly, the total effective Hamiltonian $H^{\text{ef}} = H_0^{\text{ef}} + H_B^{\text{ef}}$ is block diagonalized. In the Hilbert subspace spanned by $|e+\rangle$ and $|g-\rangle$, we have one effective two-band Hamiltonian [40]

$$H^{\text{ef}} = \frac{\hbar^2 k_z^2}{2m_h^*} + \left(C \frac{\hbar^2}{m_0 R} + Z_3 \mu_B B R \right) k_z \sigma^x + \left(\frac{\Delta}{2} \frac{\hbar^2}{m_0 R^2} + Z_1 \mu_B B + Z_4 \frac{e^2 B^2 R^2}{2m_0} \right) \sigma^z \quad (37)$$

where σ^x and σ^z are Pauli matrices defined in this Hilbert subspace. In the Hilbert subspace spanned by $|e-\rangle$ and $|g+\rangle$, we have the other effective two-band Hamiltonian [40]

$$H^{\text{ef}} = \frac{\hbar^2 k_z^2}{2m_h^*} + \left(C \frac{\hbar^2}{m_0 R} - Z_3 \mu_B B R \right) k_z \sigma^x + \left(\frac{\Delta}{2} \frac{\hbar^2}{m_0 R^2} - Z_1 \mu_B B + Z_4 \frac{e^2 B^2 R^2}{2m_0} \right) \sigma^z \quad (38)$$

These two equations (37) and (38) have the exact form as Eq. (33), and nicely explain the two sets of the combined subband dispersions I and II shown in Figs. 11(a), 12(a), and 13(a). The subband dispersions in a strong longitudinal field can indeed be classified into different spin sets! Actually, the conservation of F_z in the total Hamiltonian (31) for the longitudinal field case also implies this result. Also, these two equations show that both ‘spin’-orbit coupling α and effective g -factor g_h^* depend on the magnetic field B .

Both the ‘spin’-orbit coupling α and the effective g -factor g_h^* are plotted as a function of the longitudinal field B in Figs. 14, 15, and 16 for growth directions [001], [111], and [110], respectively. In these figures, the dashed-dot lines are the results of the set I combined dispersions, i.e., modelled by Eq. (38), and the solid lines are the results of the set II combined dispersions, i.e., modelled by Eq. (37). Because the energy gap Δ is relatively large for growth direction [001], the effective g -factor g_h^* is relatively large too (see Fig. 14(b)). The energy gap Δ is

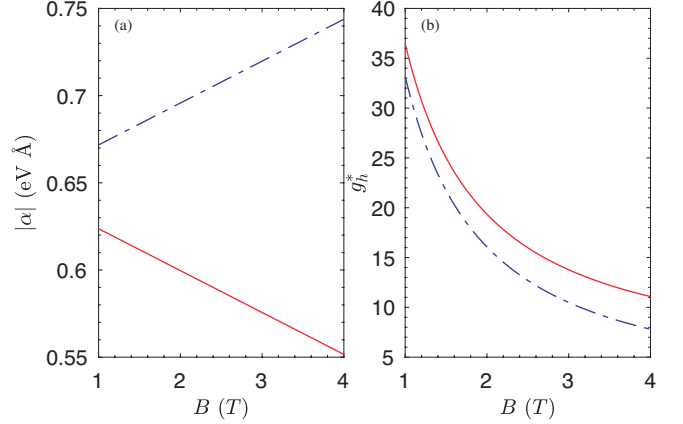


FIG. 14. The ‘spin’-orbit coupling α (a) and the effective g -factor g_h^* (b) as a function of the longitudinal field for growth direction [001]. The solid lines and the dashed-dot lines are results from Eqs. (37) and (38), respectively. We have used the fitting parameters given in the parentheses of Tab. I, and $R = 10$ nm.

negative for growth direction [111], such that the effective g -factor g_h^* is mostly negative. Moreover, the effective g -factor g_h^* of the set II combined dispersions (see Eq. (37)) can be tuned from negative to zero, and even to positive with increasing the magnetic field (see the solid line in Fig. 15(b)). The effective g -factor g_h^* is smallest (the absolute value) for growth direction [110] in comparison with the other two growth directions (see Fig. 16(b)).

The lowest combined hole subband dispersions, i.e., the set I lines shown in Figs. 11(a), 12(a), and 13(a), are involved in most applications. We find nanowires grew along the [111] direction are especially useful for the spin qubit applications, because both the ‘spin’-orbit coupling α and the Zeeman splitting $|g_h^*| \mu_B B$ increase with the longitudinal field B (see the dashed-dot lines shown in Fig. 15).

B. The strong transverse field case

When the magnetic field is applied transversely, i.e., the field $\mathbf{B} = (B, 0, 0)$ is perpendicular to the nanowire, the low-energy effective Hamiltonian of the magnetic

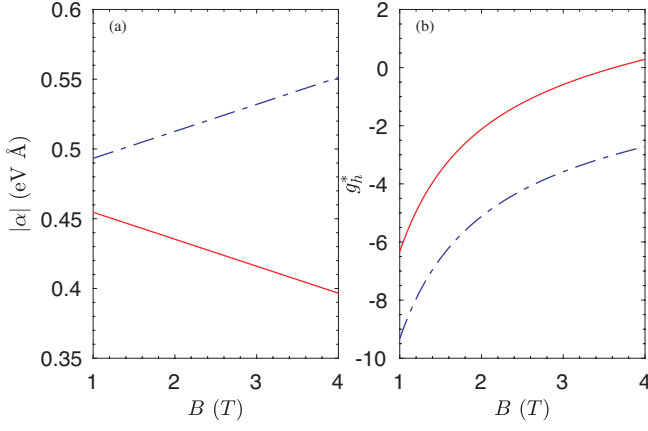


FIG. 15. The ‘spin’-orbit coupling α (a) and the effective g -factor g_h^* (b) as a function of the longitudinal field for growth direction [111]. The solid lines and the dashed-dot lines are results from Eqs. (37) and (38), respectively. We have used the fitting parameters given in the parentheses of Tab. I, and $R = 10$ nm.

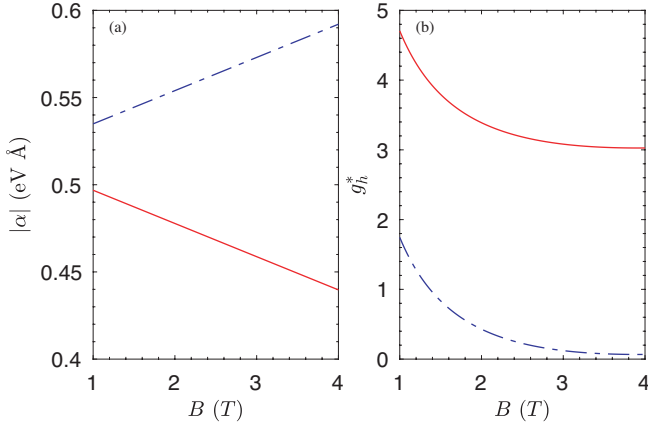


FIG. 16. The ‘spin’-orbit coupling α (a) and the effective g -factor g_h^* (b) as a function of the longitudinal field for growth direction [110]. The solid lines and the dashed-dot lines are results from Eqs. (37) and (38), respectively. We have used the fitting parameters given in the parentheses of Tab. I, and $R = 10$ nm.

term H_B in Eq. (32) now is written as [37, 40]

$$H_B^{\text{ef}} = \mu_B B (X_1 s^x + X_2 \tau^z s^x + X_3 k_z R \tau^x) + X_4 \frac{e^2 B^2 R^2}{2m_0} \tau^z, \quad (39)$$

where X_i ($i = 1, 2, 3, 4$) are parameters describing both the Zeeman and the orbital effects of the transverse magnetic field (see appendix D). The X_4 term is caused by terms proportional to B^2 . The values of $X_{1,2,3,4}$ are given in Tab. I. Now, it is more easy to find the block diagonalized feather of the total effective Hamiltonian $H^{\text{ef}} = H_0^{\text{ef}} + H_B^{\text{ef}}$ than that in the longitudinal field case, because the operator s^x is a conserved quantity here. For

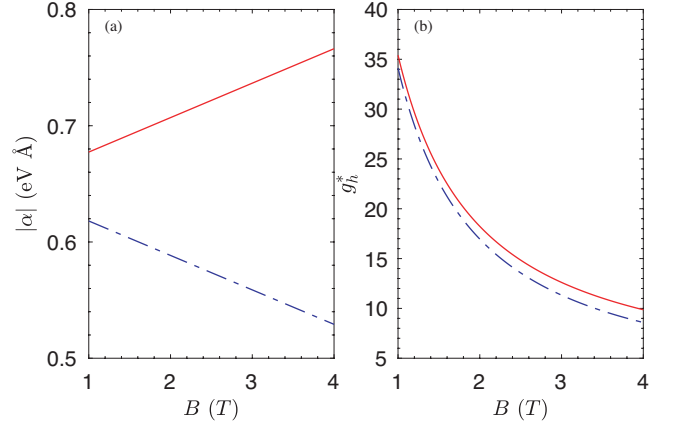


FIG. 17. The ‘spin’-orbit coupling α (a) and the effective g -factor g_h^* (b) as a function of the transverse field for growth direction [001]. The solid lines and the dashed-dot lines are results from Eqs. (40) and (41), respectively. We have used the fitting parameters given in the parentheses of Tab. I, and $R = 10$ nm.

$s^x = 1$, the total effective Hamiltonian H^{ef} reads [40]

$$H^{\text{ef}} = \frac{\hbar^2 k_z^2}{2m_h^*} + \left(C \frac{\hbar^2}{m_0 R} + X_3 \mu_B B R \right) k_z \tau^x + \left(\frac{\Delta}{2} \frac{\hbar^2}{m_0 R^2} + X_2 \mu_B B + X_4 \frac{e^2 B^2 R^2}{2m_0} \right) \tau^z \quad (40)$$

For $s^x = -1$, the total effective Hamiltonian H^{ef} reads [40]

$$H^{\text{ef}} = \frac{\hbar^2 k_z^2}{2m_h^*} - \left(C \frac{\hbar^2}{m_0 R} - X_3 \mu_B B R \right) k_z \tau^x + \left(\frac{\Delta}{2} \frac{\hbar^2}{m_0 R^2} - X_2 \mu_B B + X_4 \frac{e^2 B^2 R^2}{2m_0} \right) \tau^z \quad (41)$$

When the magnetic field is transverse, we have still recovered Eq. (33) successfully. The classification of subband dispersions into different spin sets is still feasible. These two equations (40) and (41) now nicely explain the two sets of the combined subband dispersions I and II shown in Figs. 11(b), 12(b), and 13(b).

Both the ‘spin’-orbit coupling α and the effective g -factor g_h^* are plotted as a function of the transverse field B in Figs. 17, 18, and 19 for growth directions [001], [111], and [110], respectively. In these figures, the dashed-dot lines are the results of the set I confined dispersions, i.e., modelled by Eq. (41), and the solid lines are the results of the set II combined dispersions, i.e., modelled by Eq. (40). The results in the transverse field case are very similar to that in the longitudinal field case, i.e., both α and g_h^* here have the same order of magnitudes as that in the longitudinal field case. The key difference is that, the two sets of combined subband dispersions in the transverse field case are not well separated from each other [see Figs. 11(b), 12(b), 13(b)], while they are well separated in the longitudinal field case. Therefore, the potential

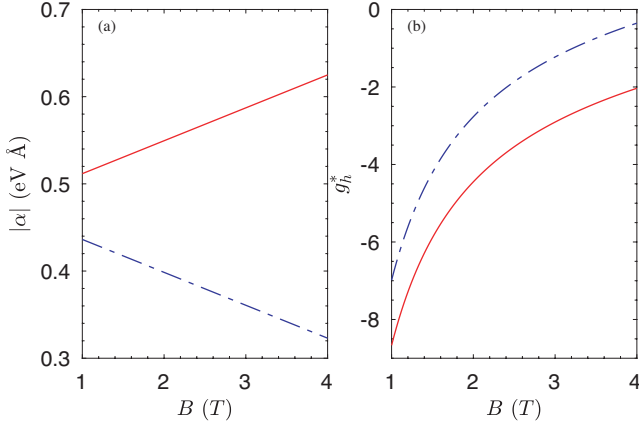


FIG. 18. The ‘spin’-orbit coupling α (a) and the effective g -factor g_h^* (b) as a function of the transverse field for growth direction [111]. The solid lines and the dashed-dot lines are results from Eqs. (40) and (41), respectively. We have used the fitting parameters given in the parentheses of Tab. I, and $R = 10$ nm.

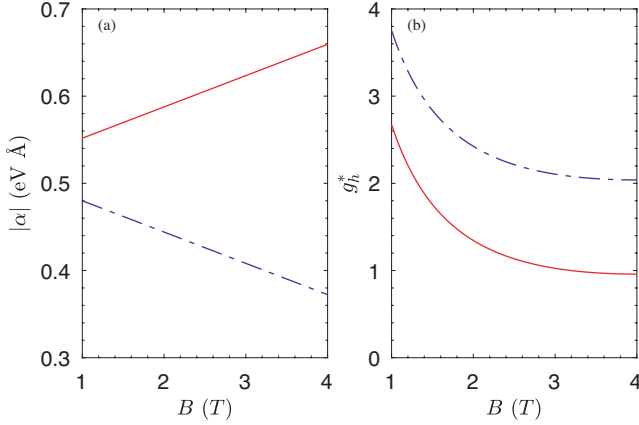


FIG. 19. The ‘spin’-orbit coupling α (a) and the effective g -factor g_h^* (b) as a function of the transverse field for growth direction [110]. The solid lines and the dashed-dot lines are results from Eqs. (40) and (41), respectively. We have used the fitting parameters given in the parentheses of Tab. I, and $R = 10$ nm.

applications of the two-band Hamiltonians (40) and (41) in a transverse field may be limited by this unsuccessful separation.

C. The transverse electric field case

A transverse external electric field can certainly lift the spin degeneracy in the hole subband dispersions. The transverse electric field breaks the inversion symmetry in the nanowire cross-section, such that the so-called Rashba spin splitting occurs at the wave vector sites $k_z R \neq 0$ [2, 19, 42]. Many papers have studied theoretically this effect in nanowires with various nanowire cross-sections [37, 43, 71, 91]. When an electric field $(E_x, 0, 0)$

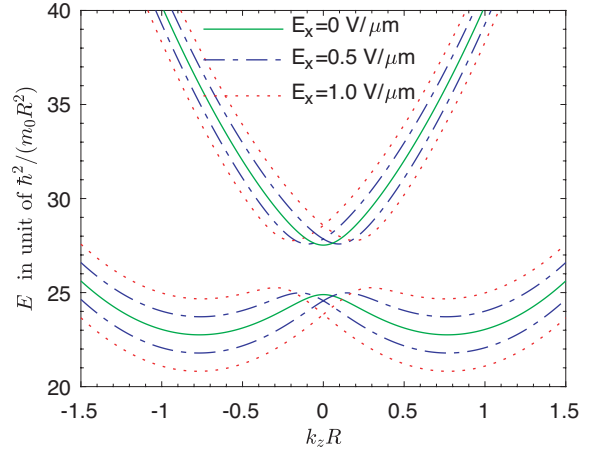


FIG. 20. Spin splitting induced by external electric field in the lowest two subband dispersions for growth direction [001]. We have used the fitting parameters given in the parentheses of Tab. I, and $R = 10$ nm.

is applied in the x direction, holes in the nanowire feel an additional electric potential energy with Hamiltonian

$$H_{ed} = -eE_x x = -eE_x r \cos \varphi. \quad (42)$$

The hole spin-orbit coupling is implicitly contained in the multi-band Hamiltonian $H = H_0 + H_{ed}$, such that we shouldn’t add an additional spin-orbit coupling term such as $\alpha_h \mathbf{E} \cdot (\mathbf{k} \times \mathbf{J})$ to the multi-band Hamiltonian. In the low-energy Hilbert subspace spanned by $|e+\rangle$, $|e-\rangle$, $|g+\rangle$, and $|g-\rangle$, we write H_{ed} as an effective Hamiltonian [37]

$$H_{ed}^{\text{ef}} = eE_x R U \tau^y s^z. \quad (43)$$

The analytical formula of parameter U is given in appendix D and its values calculated using both the spherical and the axial Luttinger-Kohn Hamiltonians are given in Tab. I.

The spin splitting induced by external electric field in the lowest two subband dispersions can be obtained by directly diagonalizing the 4×4 effective Hamiltonian $H^{\text{ef}} = H_0^{\text{ef}} + H_{ed}^{\text{ef}}$. The results of the spherical approximation were shown in Ref. [37]. The results of the axial approximation are shown in Figs. 20, 21, and 22 for growth directions [001], [111], and [110], respectively. At a first glance, the hole spin splitting induced by external electric field in quasi-one-dimension looks very unusual. It is apparently different from its quasi-two-dimensional counterpart, that is characterizable by terms such as $(k_+^3 \sigma_- - k_-^3 \sigma_+) E_z$ [2, 19]. It is also different from the spin splitting of the conduction-band electrons, where is characterized by a linear-in-momentum term $(k_- \sigma_+ - k_+ \sigma_-) E_z$ [42]. The essential reason of these differences is that the hole subband minimums in quasi-one-dimension are not located at $k_z R = 0$, the $k_z R = 0$ is an energy anticrossing site instead. However, the structure inversion asymmetry induced by external electric field must give rise to spin splittings at the wave vectors

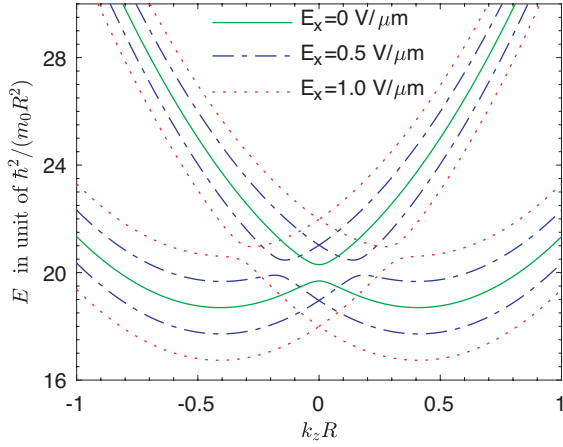


FIG. 21. Spin splitting induced by external electric field in the lowest two subband dispersions for growth direction [111]. We have used the fitting parameters given in the parentheses of Tab. I, and $R = 10$ nm.

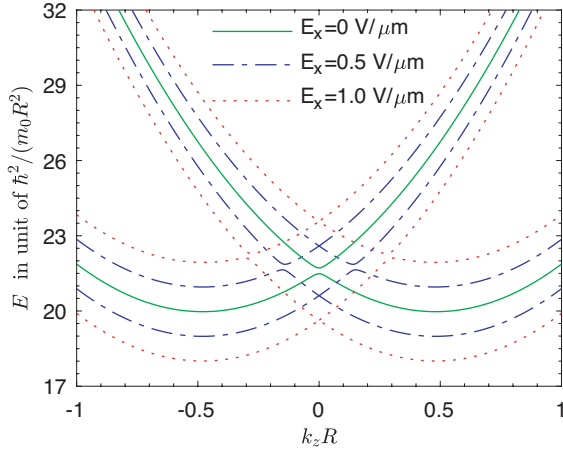


FIG. 22. Spin splitting induced by external electric field in the lowest two subband dispersions for growth direction [110]. We have used the fitting parameters given in the parentheses of Tab. I, and $R = 10$ nm.

$k_z R \neq 0$, such that strange looks of the subband dispersions with spin splitting appear in Figs. 20, 21, and 22. One can find the time-reversal symmetry is indeed hold in these figures.

For very large transverse electric fields, it is possible to describe the lowest two subband dispersions, e.g. the two shifted parabolic curves of $E_x = 1.0$ V/ μm in Fig. 22, by using an effective two-band Hamiltonian. Also, the spin-splitting now is characterizable by a linear-in momentum

term $k_z \sigma^x E_x$ [55]. However, for small transverse electric fields, a four-band effective Hamiltonian $H^{\text{ef}} = H_0^{\text{ef}} + H_{\text{ed}}^{\text{ef}}$ is necessary.

IX. DISCUSSION AND SUMMARY

A series of experiments have shown signs of very strong hole spin-orbit coupling in the Ge/Si core/shell nanowire heterostructure [70, 92], spin-orbit length as small as 20 nm [93] and even smaller value of 3 nm [94] are reported. Also, the longitudinal g -factor of hole is reported to be comparable with the transverse g -factor [94, 95]. We remark that these observations do not conflict with the concept of the hole ‘spin’ introduced in this paper. While in terms of the real hole spin, the longitudinal g -factor should be much smaller than the transverse g -factor [37, 73].

The ‘spin’-orbit coupling stems from the peculiar double-well anticrossing subband structure of the quasi-one-dimensional hole gas. If a strain term proportional to J_z^2 [44, 45, 96] is added to Hamiltonian (5), the low-energy double-well subband structure will disappear. The lowest subband dispersion will become a single-well parabolic curve, and the ‘spin’-orbit coupling is destroyed as well. In this sense, the theoretical results of our paper are suitable to relaxed nanowires.

In summary, we have briefly reviewed both the theoretical method in calculating the subband dispersions and the construction of the low-energy effective Hamiltonian of the quasi-one-dimensional hole gas. A series of analytical formulas are derived in terms of the Luttinger-Kohn Hamiltonian in the axial approximation. The axial approximation gives rise to high accurate subband dispersions for both growth directions [001] and [111]. It is possible to obtain two sets of combined dispersions with strong ‘spin’-orbit coupling and isolated from each other by lifting the spin degeneracy in the subband dispersions. We further construct the low-energy effective Hamiltonians of the hole gas in the absence and presence of external magnetic field. Both the double-well anticrossing subband structure and the classification of the subband dispersions into spin sets are qualitatively captured in these effective Hamiltonians.

We expect the strong ‘spin’-orbit coupling achieved in a strong magnetic field has broad applications in quantum computing, e.g., the electrical manipulation of the hole spin and spin-cavity interaction etc. Also, the potential consequences of the quantum state inversion occurred between direction [001]/[110] and [111] are still waiting for further studies.

Appendix A: Matrices of operators $J_{x,y,z}$ and $\Gamma_{1,3}$

In this paper, the matrices of operators $J_{x,y,z}$ and $\Gamma_{1,3}$ are as follows:

$$\begin{aligned}
 J_x &= \begin{pmatrix} 0 & \frac{\sqrt{3}}{2} & 0 & 0 \\ \frac{\sqrt{3}}{2} & 0 & 1 & 0 \\ 0 & 1 & 0 & \frac{\sqrt{3}}{2} \\ 0 & 0 & \frac{\sqrt{3}}{2} & 0 \end{pmatrix}, \quad J_y = \begin{pmatrix} 0 & -i\frac{\sqrt{3}}{2} & 0 & 0 \\ i\frac{\sqrt{3}}{2} & 0 & -i & 0 \\ 0 & i & 0 & -i\frac{\sqrt{3}}{2} \\ 0 & 0 & i\frac{\sqrt{3}}{2} & 0 \end{pmatrix}, \quad J_z = \begin{pmatrix} \frac{3}{2} & 0 & 0 & 0 \\ 0 & \frac{1}{2} & 0 & 0 \\ 0 & 0 & -\frac{1}{2} & 0 \\ 0 & 0 & 0 & -\frac{3}{2} \end{pmatrix}, \\
 \Gamma_1 &= \begin{pmatrix} 0 & 0 & i & 0 \\ 0 & 0 & 0 & i \\ -i & 0 & 0 & 0 \\ 0 & -i & 0 & 0 \end{pmatrix}, \quad \Gamma_3 = \begin{pmatrix} 0 & -i & 0 & 0 \\ i & 0 & 0 & 0 \\ 0 & 0 & 0 & i \\ 0 & 0 & -i & 0 \end{pmatrix}.
 \end{aligned} \tag{A1}$$

Appendix B: The equation array of the coefficients $c_{1,2,3,4}$

The hard-wall boundary condition $\Psi(R, \varphi, z) = 0$ can be written as

$$\begin{aligned}
 \frac{2i\tilde{\gamma}_2 k_z}{\tilde{\gamma}_3 \mu_1} J_{m-1}(\mu_1 R) c_1 + \frac{\tilde{\gamma}_1(\mu_1^2 - 2k_z^2) \pm \chi_{\mu_1}}{\sqrt{3}\tilde{\gamma}_3 \mu_1^2} J_{m-1}(\mu_1 R) c_2 + \frac{2i\tilde{\gamma}_2 k_z}{\tilde{\gamma}_3 \mu_2} J_{m-1}(\mu_2 R) c_3 + \frac{\tilde{\gamma}_1(\mu_2^2 - 2k_z^2) - \chi_{\mu_2}}{\sqrt{3}\tilde{\gamma}_3 \mu_2^2} J_{m-1}(\mu_2 R) c_4 &= 0, \\
 \frac{-\tilde{\gamma}_1(\mu_1^2 - 2k_z^2) \pm \chi_{\mu_1}}{\sqrt{3}\tilde{\gamma}_3 \mu_1^2} J_m(\mu_1 R) c_1 - \frac{2i\tilde{\gamma}_2 k_z}{\tilde{\gamma}_3 \mu_1} J_m(\mu_1 R) c_2 - \frac{\tilde{\gamma}_1(\mu_2^2 - 2k_z^2) + \chi_{\mu_2}}{\sqrt{3}\tilde{\gamma}_3 \mu_2^2} J_m(\mu_2 R) c_3 - \frac{2i\tilde{\gamma}_2 k_z}{\tilde{\gamma}_3 \mu_2} J_m(\mu_2 R) c_4 &= 0, \\
 J_{m+1}(\mu_1 R) c_2 + J_{m+1}(\mu_2 R) c_4 &= 0, \\
 J_{m+2}(\mu_1 R) c_1 + J_{m+2}(\mu_2 R) c_3 &= 0.
 \end{aligned} \tag{B1}$$

At the site $k_z = 0$, the boundary condition is reduced to

$$\begin{aligned}
 \frac{\tilde{\gamma}_1 \pm \sqrt{\tilde{\gamma}_1^2 + 3\tilde{\gamma}_3^2}}{\sqrt{3}\tilde{\gamma}_3} J_{m-1}(\mu_1 R) c_2 + \frac{\tilde{\gamma}_1 - \sqrt{\tilde{\gamma}_1^2 + 3\tilde{\gamma}_3^2}}{\sqrt{3}\tilde{\gamma}_3} J_{m-1}(\mu_2 R) c_4 &= 0, \\
 \frac{-\tilde{\gamma}_1 \pm \sqrt{\tilde{\gamma}_1^2 + 3\tilde{\gamma}_3^2}}{\sqrt{3}\tilde{\gamma}_3} J_m(\mu_1 R) c_1 - \frac{\tilde{\gamma}_1 + \sqrt{\tilde{\gamma}_1^2 + 3\tilde{\gamma}_3^2}}{\sqrt{3}\tilde{\gamma}_3} J_m(\mu_2 R) c_3 &= 0, \\
 J_{m+1}(\mu_1 R) c_2 + J_{m+1}(\mu_2 R) c_4 &= 0, \\
 J_{m+2}(\mu_1 R) c_1 + J_{m+2}(\mu_2 R) c_3 &= 0.
 \end{aligned} \tag{B2}$$

One can see the equations of c_1 and c_3 are decoupled from the equations of c_2 and c_4 . The equations of c_1 and c_3 give rise to Eq. (25), and the equations of c_2 and c_4 give rise to Eq. (24).

Appendix C: The perturbation term H_B

When a strong magnetic field $\mathbf{B} = (B_x, 0, B_z)$ is applied, we make the following replacements in Eq. (31)

$$k'_x = -i\partial_x - \frac{eB_z}{2\hbar} r \sin \varphi, \quad k'_y = -i\partial_y + \frac{eB_z}{2\hbar} r \sin \varphi, \quad k'_z = -i\partial_z + \frac{eB_x}{\hbar} r \sin \varphi. \tag{C1}$$

For obtaining the orbital effects of the magnetic field, we first calculate the following terms

$$\begin{aligned}
 k_x'^2 + k_y'^2 &= k_x^2 + k_y^2 - i\frac{eB_z}{\hbar} \partial_\varphi + \frac{e^2 B_z^2 r^2}{4\hbar^2}, \\
 k_z'^2 &= k_z^2 + 2\frac{eB_x}{\hbar} k_z r \sin \varphi + \frac{e^2 B_x^2}{\hbar^2} r^2 \sin^2 \varphi, \\
 \{k'_z, k'_-\} &= \{k_z, k_-\} - \frac{eB_x}{\hbar} \left(\frac{1}{2} + \sin \varphi e^{-i\varphi} (ir\partial_r + \partial_\varphi) \right) - i\frac{eB_z}{2\hbar} k_z r e^{-i\varphi} - i\frac{e^2 B_x B_z}{2\hbar^2} r^2 \sin \varphi e^{-i\varphi}, \\
 k_-'^2 &= k_-^2 - \frac{eB_z}{\hbar} (r\partial_r e^{-2i\varphi} - i e^{-2i\varphi} \partial_\varphi) - \frac{e^2 B_z^2 r^2}{4\hbar^2} e^{-2i\varphi}.
 \end{aligned} \tag{C2}$$

Interested readers can also refer to Ref. [43]. Now the perturbation term H_B in Eq. (32) can be written as

$$H_B = \frac{\hbar^2}{2m_0} \begin{pmatrix} F' & S' & I' & 0 \\ S'^{\dagger} & G' & 0 & I' \\ I'^{\dagger} & 0 & G' & -S' \\ 0 & I'^{\dagger} & -S'^{\dagger} & F' \end{pmatrix} + 2\kappa\mu_B \mathbf{B} \cdot \mathbf{J}, \quad (\text{C3})$$

where

$$\begin{aligned} F' &= (\gamma_1 + \tilde{\gamma}_1) \left(-i \frac{eB_z}{\hbar} \partial_\varphi + \frac{e^2 B_z^2 r^2}{4\hbar^2} \right) + (\gamma_1 - 2\tilde{\gamma}_1) \left(2 \frac{eB_x}{\hbar} k_z r \sin \varphi + \frac{e^2 B_x^2 r^2}{\hbar^2} \sin^2 \varphi \right), \\ G' &= (\gamma_1 - \tilde{\gamma}_1) \left(-i \frac{eB_z}{\hbar} \partial_\varphi + \frac{e^2 B_z^2 r^2}{4\hbar^2} \right) + (\gamma_1 + 2\tilde{\gamma}_1) \left(2 \frac{eB_x}{\hbar} k_z r \sin \varphi + \frac{e^2 B_x^2 r^2}{\hbar^2} \sin^2 \varphi \right), \\ S' &= -2\sqrt{3}\tilde{\gamma}_2 \left(-\frac{eB_x}{\hbar} \left(\frac{1}{2} + \sin \varphi e^{-i\varphi} (ir\partial_r + \partial_\varphi) \right) - i \frac{eB_z}{2\hbar} k_z r e^{-i\varphi} - i \frac{e^2 B_x B_z}{2\hbar^2} r^2 \sin \varphi e^{-i\varphi} \right), \\ I' &= -\sqrt{3}\tilde{\gamma}_3 \left(-\frac{eB_z}{\hbar} (r\partial_r e^{-2i\varphi} - i e^{-2i\varphi} \partial_\varphi) - \frac{e^2 B_z^2 r^2}{4\hbar^2} e^{-2i\varphi} \right). \end{aligned} \quad (\text{C4})$$

For a longitudinal field we set $B_x = 0$ and for a transverse field we set $B_z = 0$ in Eq. (C3).

Appendix D: The parameters of the low-energy effective Hamiltonian

The low-energy Hilbert subspace is spanned by the lowest four eigenstates of $H_0|_{k_z=0}$, i.e.,

$$|g-\rangle = \begin{pmatrix} 0 \\ \Psi_{I,2}(r) \\ 0 \\ \Psi_{I,4}(r)e^{2i\varphi} \end{pmatrix}, \quad |g+\rangle = \begin{pmatrix} \Psi_{I,4}^*(r)e^{-2i\varphi} \\ 0 \\ \Psi_{I,2}^*(r) \\ 0 \end{pmatrix}, \quad |e-\rangle = \begin{pmatrix} 0 \\ \Psi_{II,3}^*(r)e^{-i\varphi} \\ 0 \\ \Psi_{II,1}^*(r)e^{i\varphi} \end{pmatrix}, \quad |e+\rangle = \begin{pmatrix} \Psi_{II,1}(r)e^{-i\varphi} \\ 0 \\ \Psi_{II,3}(r)e^{i\varphi} \\ 0 \end{pmatrix} \quad (\text{D1})$$

The corresponding coefficients $c_{1,2,3,4}$ in $\Psi_I(r)$ and $\Psi_{II}(r)$ are easily obtainable (see Eqs. (26) and (27)). After some tedious algebra, the parameters of the low-energy effective Hamiltonian can be derived as

$$\begin{aligned} m_e^* &= \frac{m_0}{2\pi \int_0^R dr r \left((\gamma_1 - 2\tilde{\gamma}_1) |\Psi_{II,1}(r)|^2 + (\gamma_1 + 2\tilde{\gamma}_1) |\Psi_{II,3}(r)|^2 \right)}, \\ m_g^* &= \frac{m_0}{2\pi \int_0^R dr r \left((\gamma_1 + 2\tilde{\gamma}_1) |\Psi_{I,2}(r)|^2 + (\gamma_1 - 2\tilde{\gamma}_1) |\Psi_{I,4}(r)|^2 \right)}, \\ C &= \sqrt{3}\tilde{\gamma}_2 R \int_0^R dr r \int_0^{2\pi} d\varphi \left(-\Psi_{I,2}^*(r) k_+ \Psi_{II,1}(r) e^{-i\varphi} + \Psi_{I,4}^*(r) e^{-2i\varphi} k_+ \Psi_{II,3}(r) e^{i\varphi} \right), \\ Z_1 &= 2\pi\kappa \int_0^R dr r \left(\frac{3}{2} |\Psi_{II,1}(r)|^2 - \frac{1}{2} |\Psi_{II,3}(r)|^2 - \frac{1}{2} |\Psi_{I,2}(r)|^2 + \frac{3}{2} |\Psi_{I,4}(r)|^2 \right) \\ &\quad + \pi \int_0^R dr r \left(-(\gamma_1 + \tilde{\gamma}_1) |\Psi_{II,1}(r)|^2 + (\gamma_1 - \tilde{\gamma}_1) |\Psi_{II,3}(r)|^2 - 2(\gamma_1 + \tilde{\gamma}_1) |\Psi_{I,4}(r)|^2 \right) \\ &\quad + \pi\sqrt{3}\tilde{\gamma}_3 \int_0^R dr r \left(\Psi_{II,1}^*(r) (r\partial_r + 1) \Psi_{II,3}(r) - \Psi_{I,2}^*(r) (r\partial_r + 2) \Psi_{I,4}(r) + c.c. \right), \\ Z_2 &= 2\pi\kappa \int_0^R dr r \left(\frac{3}{2} |\Psi_{II,1}(r)|^2 - \frac{1}{2} |\Psi_{II,3}(r)|^2 + \frac{1}{2} |\Psi_{I,2}(r)|^2 - \frac{3}{2} |\Psi_{I,4}(r)|^2 \right) \\ &\quad + \pi \int_0^R dr r \left(-(\gamma_1 + \tilde{\gamma}_1) |\Psi_{II,1}(r)|^2 + (\gamma_1 - \tilde{\gamma}_1) |\Psi_{II,3}(r)|^2 + 2(\gamma_1 + \tilde{\gamma}_1) |\Psi_{I,4}(r)|^2 \right) \\ &\quad + \pi\sqrt{3}\tilde{\gamma}_3 \int_0^R dr r \left(\Psi_{II,1}^*(r) (r\partial_r + 1) \Psi_{II,3}(r) + \Psi_{I,2}^*(r) (r\partial_r + 2) \Psi_{I,4}(r) + c.c. \right), \\ Z_3 &= (2\pi\sqrt{3}\tilde{\gamma}_2/R) \int_0^R dr r \left(-ir \Psi_{I,2}^*(r) \Psi_{II,1}(r) + ir \Psi_{I,4}^*(r) \Psi_{II,3}(r) \right), \end{aligned}$$

$$\begin{aligned}
Z_4 &= \pi(\gamma_1 + \frac{5}{2}\tilde{\gamma}_1)\frac{1}{4R^2} \int_0^R dr r^3 \left(|\Psi_{II,1}(r)|^2 + |\Psi_{II,3}(r)|^2 - |\Psi_{I,2}(r)|^2 - |\Psi_{I,4}(r)|^2 \right) \\
&\quad - \frac{\pi}{2R^2} \int_0^R dr r^3 \left(-\frac{\sqrt{3}}{2}\tilde{\gamma}_3(\Psi_{II,1}^*(r)\Psi_{II,3}(r) - \Psi_{I,2}^*(r)\Psi_{I,4}(r)) - \frac{\sqrt{3}}{2}\tilde{\gamma}_3(\Psi_{II,3}^*(r)\Psi_{II,1}(r) - \Psi_{I,4}^*(r)\Psi_{I,2}(r)) \right. \\
&\quad \left. + \frac{3}{4}\tilde{\gamma}_1(|\Psi_{II,1}(r)|^2 - |\Psi_{I,4}(r)|^2) + \frac{7}{4}\tilde{\gamma}_1(|\Psi_{II,3}(r)|^2 - |\Psi_{I,2}(r)|^2) \right), \\
X_1 &= 2\pi\kappa \int_0^R dr r \left(\sqrt{3}\Psi_{II,1}^*(r)\Psi_{II,3}^*(r) + \Psi_{I,2}^*(r)\Psi_{I,2}^*(r) \right) \\
&\quad + 2\pi\sqrt{3}\tilde{\gamma}_2 \int_0^R dr r \left(\Psi_{II,1}^*(r)(r\partial_r + 1)\Psi_{II,3}^*(r) - \Psi_{II,1}^*(r)\Psi_{II,3}^*(r) + \Psi_{I,2}^*(r)(r\partial_r + 2)\Psi_{I,4}^*(r) \right), \\
X_2 &= 2\pi\kappa \int_0^R dr r \left(\sqrt{3}\Psi_{II,1}^*(r)\Psi_{II,3}^*(r) - \Psi_{I,2}^*(r)\Psi_{I,2}^*(r) \right) \\
&\quad + 2\pi\sqrt{3}\tilde{\gamma}_2 \int_0^R dr r \left(\Psi_{II,1}^*(r)(r\partial_r + 1)\Psi_{II,3}^*(r) - \Psi_{II,1}^*(r)\Psi_{II,3}^*(r) - \Psi_{I,2}^*(r)(r\partial_r + 2)\Psi_{I,4}^*(r) \right), \\
X_3 &= -(2i\pi/R) \int_0^R dr r^2 \left((\gamma_1 + 2\tilde{\gamma}_1)\Psi_{I,2}^*(r)\Psi_{II,3}^*(r) + (\gamma_1 - 2\tilde{\gamma}_1)\Psi_{I,4}^*(r)\Psi_{II,1}^*(r) \right), \\
X_4 &= \frac{\pi}{2R^2} \int_0^R dr r^3 \left((\gamma_1 - 2\tilde{\gamma}_1)(|\Psi_{II,1}(r)|^2 - |\Psi_{I,4}(r)|^2) + (\gamma_1 + 2\tilde{\gamma}_1)(|\Psi_{II,3}(r)|^2 - |\Psi_{I,2}(r)|^2) \right), \\
U &= -(i\pi/R) \int_0^R dr r^2 \left(\Psi_{I,2}^*(r)\Psi_{II,3}^*(r) + \Psi_{I,4}^*(r)\Psi_{II,1}^*(r) \right). \tag{D2}
\end{aligned}$$

Here *c.c.* means taking the complex conjugate of the preceding terms.

-
- [1] G. L. Bir, G. E. Pikus, and D. Louvish, *Symmetry and strain-induced effects in semiconductors*, Vol. 484 (Wiley New York, 1974).
- [2] R. Winkler, *Spin-Orbit Coupling Effects in Two-Dimensional Electron and Hole Systems* (Springer, Berlin, 2003).
- [3] Y. Sun, S. E. Thompson, and T. Nishida, *Strain effect in semiconductors: theory and device applications* (Springer Science & Business Media, New York, 2009).
- [4] E. O. Kane, Band structure of indium antimonide, *Journal of Physics and Chemistry of Solids* **1**, 249 (1957).
- [5] J. M. Luttinger and W. Kohn, Motion of electrons and holes in perturbed periodic fields, *Phys. Rev.* **97**, 869 (1955).
- [6] E. Bangert and G. Landwehr, Self-consistent calculations of electric subbands in p-type GaAlAs-GaAs heterojunctions, *Superlattices and Microstructures* **1**, 363 (1985).
- [7] B. A. Foreman, Effective-mass hamiltonian and boundary conditions for the valence bands of semiconductor microstructures, *Phys. Rev. B* **48**, 4964 (1993).
- [8] C. Y.-P. Chao and S. L. Chuang, Spin-orbit-coupling effects on the valence-band structure of strained semiconductor quantum wells, *Phys. Rev. B* **46**, 4110 (1992).
- [9] R. Winkler, M. Merkler, T. Darnhofer, and U. Rössler, Theory for the cyclotron resonance of holes in strained asymmetric Ge-SiGe quantum wells, *Phys. Rev. B* **53**, 10858 (1996).
- [10] D. A. Broido and L. J. Sham, Effective masses of holes at GaAs-AlGaAs heterojunctions, *Phys. Rev. B* **31**, 888 (1985).
- [11] E. Rashba and E. Sherman, Spin-orbital physics splitting in symmetric quantum wells, *Physics Letters A* **129**, 175 (1988).
- [12] L. C. Andreani, A. Pasquarello, and F. Bassani, Hole subbands in strained GaAs-Ga_{1-x}Al_xAs quantum wells: Exact solution of the effective-mass equation, *Phys. Rev. B* **36**, 5887 (1987).
- [13] S. L. Chuang, Efficient band-structure calculations of strained quantum wells, *Phys. Rev. B* **43**, 9649 (1991).
- [14] J. M. Luttinger, Quantum theory of cyclotron resonance in semiconductors: General theory, *Phys. Rev.* **102**, 1030 (1956).
- [15] R. Oberhuber, G. Zandler, and P. Vogl, Subband structure and mobility of two-dimensional holes in strained Si/SiGe MOSFET's, *Phys. Rev. B* **58**, 9941 (1998).
- [16] T. Ando, Hole subband at GaAs/AlGaAs heterojunctions and quantum wells, *Journal of the physical society of Japan* **54**, 1528 (1985).
- [17] U. Ekenberg and M. Altarelli, Subbands and landau levels in the two-dimensional hole gas at the GaAs-Al_xGa_{1-x}As interface, *Phys. Rev. B* **32**, 3712 (1985).
- [18] G. Bastard and J. Brum, Electronic states in semiconductor heterostructures, *IEEE Journal of Quantum Electronics* **22**, 1625 (1986).
- [19] R. Winkler, Rashba spin splitting in two-dimensional electron and hole systems, *Phys. Rev. B* **62**, 4245 (2000).
- [20] R. Winkler, H. Noh, E. Tutuc, and M. Shayegan, Anoma-

- lous rashba spin splitting in two-dimensional hole systems, *Phys. Rev. B* **65**, 155303 (2002).
- [21] E. Marcellina, A. R. Hamilton, R. Winkler, and D. Culcer, Spin-orbit interactions in inversion-asymmetric two-dimensional hole systems: A variational analysis, *Phys. Rev. B* **95**, 075305 (2017).
- [22] M. Altarelli, U. Ekenberg, and A. Fasolino, Calculations of hole subbands in semiconductor quantum wells and superlattices, *Phys. Rev. B* **32**, 5138 (1985).
- [23] F. Schäffler, High-mobility Si and Ge structures, *Semiconductor Science and Technology*, **12**, 1515 (1997).
- [24] M. Wu, J. Jiang, and M. Weng, Spin dynamics in semiconductors, *Physics Reports* **493**, 61 (2010).
- [25] G. Scappucci, C. Kloeffel, F. A. Zwanenburg, D. Loss, M. Myronov, J.-J. Zhang, S. De Franceschi, G. Katsaros, and M. Veldhorst, The germanium quantum information route, *Nature Reviews Materials* **6**, 926 (2021).
- [26] J. Xiang, W. Lu, Y. Hu, Y. Wu, H. Yan, and C. M. Lieber, Ge/si nanowire heterostructures as high-performance field-effect transistors, *Nature* **441**, 489 (2006).
- [27] V. S. Pribiag, S. Nadj-Perge, S. M. Frolov, J. W. G. van den Berg, I. van Weperen, S. R. Plissard, E. P. A. M. Bakkers, and L. P. Kouwenhoven, Electrical control of single hole spins in nanowire quantum dots, *Nature Nanotechnology* **8**, 170 (2013).
- [28] W. Lu, J. Xiang, B. P. Timko, Y. Wu, and C. M. Lieber, One-dimensional hole gas in germanium/silicon nanowire heterostructures, *Proceedings of the National Academy of Sciences* **102**, 10046 (2005).
- [29] F. Gao, J.-H. Wang, H. Watzinger, H. Hu, M. J. Rančić, J.-Y. Zhang, T. Wang, Y. Yao, G.-L. Wang, J. Kukučka, L. Vukušić, C. Kloeffel, D. Loss, F. Liu, G. Katsaros, and J.-J. Zhang, Site-controlled uniform Ge/Si hut wires with electrically tunable spin-orbit coupling, *Advanced Materials* **32**, 1906523 (2020).
- [30] M. Brauns, J. Ridderbos, A. Li, W. G. van der Wiel, E. P. A. M. Bakkers, and F. A. Zwanenburg, Highly tuneable hole quantum dots in Ge-Si core-shell nanowires, *Applied Physics Letters* **109**, 143113 (2016).
- [31] M. Brauns, J. Ridderbos, A. Li, E. P. A. M. Bakkers, W. G. van der Wiel, and F. A. Zwanenburg, Anisotropic pauli spin blockade in hole quantum dots, *Phys. Rev. B* **94**, 041411 (2016).
- [32] P. C. Sercel and K. J. Vahala, Analytical formalism for determining quantum-wire and quantum-dot band structure in the multiband envelope-function approximation, *Phys. Rev. B* **42**, 3690 (1990).
- [33] M. Sweeny, J. Xu, and M. Shur, Hole subbands in one-dimensional quantum well wires, *Superlattices and Microstructures* **4**, 623 (1988).
- [34] R. Li, Hole subband dispersions in a cylindrical Ge nanowire: exact results based on the axial Luttinger-Kohn Hamiltonian, *Journal of Physics: Condensed Matter*, **36**, 235301 (2024).
- [35] K. Suzuki and J. C. Hensel, Quantum resonances in the valence bands of germanium. I. Theoretical considerations, *Phys. Rev. B* **9**, 4184 (1974).
- [36] H. R. Trebin, U. Rössler, and R. Ranvaud, Quantum resonances in the valence bands of zincblende semiconductors. I. Theoretical aspects, *Phys. Rev. B* **20**, 686 (1979).
- [37] C. Kloeffel, M. Trif, and D. Loss, Strong spin-orbit interaction and helical hole states in Ge/Si nanowires, *Phys. Rev. B* **84**, 195314 (2011).
- [38] R. Li, Low-energy subband wave-functions and effective g-factor of one-dimensional hole gas, *Journal of Physics: Condensed Matter* **33**, 355302 (2021).
- [39] R. Li, Searching strong ‘spin’-orbit coupled one-dimensional hole gas in strong magnetic fields, *Journal of Physics: Condensed Matter* **34**, 075301 (2022).
- [40] R. Li and X.-Y. Qi, Two-band description of the strong ‘spin’-orbit coupled one-dimensional hole gas in a cylindrical Ge nanowire, *Journal of Physics: Condensed Matter*, **35**, 135302 (2023).
- [41] R. Li and Z.-Q. Li, Low-energy hole subband dispersions in a cylindrical Ge nanowire: the effects of the nanowire growth direction, *Journal of Physics: Condensed Matter*, **35**, 345301 (2023).
- [42] Y. A. Bychkov and E. I. Rashba, Oscillatory effects and the magnetic susceptibility of carriers in inversion layers, *Journal of Physics C: Solid State Physics* **17**, 6039 (1984).
- [43] C. Kloeffel, M. J. Rančić, and D. Loss, Direct rashba spin-orbit interaction in Si and Ge nanowires with different growth directions, *Phys. Rev. B* **97**, 235422 (2018).
- [44] C. Adelsberger, M. Benito, S. Bosco, J. Klinovaja, and D. Loss, Hole-spin qubits in Ge nanowire quantum dots: Interplay of orbital magnetic field, strain, and growth direction, *Phys. Rev. B* **105**, 075308 (2022).
- [45] C. Adelsberger, S. Bosco, J. Klinovaja, and D. Loss, Enhanced orbital magnetic field effects in Ge hole nanowires, *Phys. Rev. B* **106**, 235408 (2022).
- [46] J.-W. Luo, S.-S. Li, and A. Zunger, Rapid transition of the hole rashba effect from strong field dependence to saturation in semiconductor nanowires, *Phys. Rev. Lett.* **119**, 126401 (2017).
- [47] K. Wang, G. Xu, F. Gao, H. Liu, R.-L. Ma, X. Zhang, Z. Wang, G. Cao, T. Wang, J.-J. Zhang, D. Culcer, X. Hu, H.-W. Jiang, H.-O. Li, G.-C. Guo, and G.-P. Guo, Ultrafast coherent control of a hole spin qubit in a germanium quantum dot, *Nature Communications* **13**, 206 (2022).
- [48] B. Venitucci and Y.-M. Niquet, Simple model for electrical hole spin manipulation in semiconductor quantum dots: Impact of dot material and orientation, *Phys. Rev. B* **99**, 115317 (2019).
- [49] V. P. Michal, B. Venitucci, and Y.-M. Niquet, Longitudinal and transverse electric field manipulation of hole spin-orbit qubits in one-dimensional channels, *Phys. Rev. B* **103**, 045305 (2021).
- [50] M. Milivojević, Electrical control of the hole spin qubit in Si and Ge nanowire quantum dots, *Phys. Rev. B* **104**, 235304 (2021).
- [51] R. Li and H. Zhang, Electrical manipulation of a hole ‘spin’-orbit qubit in nanowire quantum dot: The nontrivial magnetic field effects, *Chinese Physics B*, **32**, 030308 (2023).
- [52] C. Kloeffel, M. Trif, P. Stano, and D. Loss, Circuit QED with hole-spin qubits in Ge/Si nanowire quantum dots, *Phys. Rev. B* **88**, 241405 (2013).
- [53] R. Li, Spin-photon interaction in a nanowire quantum dot with asymmetrical confining potential, *Journal of Physics: Condensed Matter* **36**, 195302 (2024).
- [54] Y. Li, S.-X. Li, F. Gao, H.-O. Li, G. Xu, K. Wang, D. Liu, G. Cao, M. Xiao, T. Wang, J.-J. Zhang, G.-C. Guo, and G.-P. Guo, Coupling a germanium hut wire hole quantum dot to a superconducting microwave resonator, *Nano Letters* **18**, 2091 (2018).

- [55] F. Maier, J. Klinovaja, and D. Loss, Majorana fermions in Ge/Si hole nanowires, *Phys. Rev. B* **90**, 195421 (2014).
- [56] C. Adelsberger, H. F. Legg, D. Loss, and J. Klinovaja, Microscopic analysis of proximity-induced superconductivity and metallization effects in superconductor-germanium hole nanowires, *Phys. Rev. B* **108**, 155433 (2023).
- [57] K. Laubscher, J. D. Sau, and S. Das Sarma, Majorana zero modes in gate-defined germanium hole nanowires, *Phys. Rev. B* **109**, 035433 (2024).
- [58] Y. Hu, F. Kuemmeth, C. M. Lieber, and C. M. Marcus, Hole spin relaxation in ge-si core-shell nanowire qubits, *Nature Nanotechnology* **7**, 47 (2012).
- [59] F. Maier, C. Kloeffel, and D. Loss, Tunable g factor and phonon-mediated hole spin relaxation in Ge/Si nanowire quantum dots, *Phys. Rev. B* **87**, 161305 (2013).
- [60] O. Madelung, *Semiconductors: data handbook* (Springer Science & Business Media, 2004).
- [61] P. Lawaetz, Valence-band parameters in cubic semiconductors, *Phys. Rev. B* **4**, 3460 (1971).
- [62] J.-B. Xia, Effective-mass theory for superlattices grown on (11n)-oriented substrates, *Phys. Rev. B* **43**, 9856 (1991).
- [63] G. Liao, N. Luo, Z. Yang, K. Chen, and H. Q. Xu, Electronic structures of [001]- and [111]-oriented InSb and GaSb free-standing nanowires, *Journal of Applied Physics* **118**, 094308 (2015).
- [64] N. Luo, G. Liao, and H. Q. Xu, k.p theory of free-standing narrow band gap semiconductor nanowires, *AIP Advances* **6**, 125109 (2016).
- [65] H. Saidi and S. Ridene, Design considerations of al-gainas quaternary nanowires for mid-infrared applications, *Chemical Physics Letters* **738**, 136872 (2020).
- [66] A. Vezzosi, A. Bertoni, and G. Goldoni, Band structure of n - and p -doped core-shell nanowires, *Phys. Rev. B* **105**, 245303 (2022).
- [67] Y. M. Niquet, A. Lherbier, N. H. Quang, M. V. Fernández-Serra, X. Blase, and C. Delerue, Electronic structure of semiconductor nanowires, *Phys. Rev. B* **73**, 165319 (2006).
- [68] A. Baldereschi and N. O. Lipari, Spherical model of shallow acceptor states in semiconductors, *Phys. Rev. B* **8**, 2697 (1973).
- [69] J.-B. Xia, Electronic structures of zero-dimensional quantum wells, *Phys. Rev. B* **40**, 8500 (1989).
- [70] S. Roddaro, A. Fuhrer, P. Brusheim, C. Fasth, H. Q. Xu, L. Samuelson, J. Xiang, and C. M. Lieber, Spin states of holes in Ge/Si nanowire quantum dots, *Phys. Rev. Lett.* **101**, 186802 (2008).
- [71] H. Watzinger, C. Kloeffel, L. Vukušić, M. D. Rossell, V. Sessi, J. Kukučka, R. Kirchschrager, E. Lausecker, A. Truhlar, M. Glaser, A. Rastelli, A. Fuhrer, D. Loss, and G. Katsaros, Heavy-hole states in germanium hut wires, *Nano Letters* **16**, 6879 (2016).
- [72] T. Zhang, H. Liu, F. Gao, G. Xu, K. Wang, X. Zhang, G. Cao, T. Wang, J. Zhang, X. Hu, H.-O. Li, and G.-P. Guo, Anisotropic g -factor and spin-orbit field in a germanium hut wire double quantum dot, *Nano Letters* **21**, 3835 (2021).
- [73] M. Brauns, J. Ridderbos, A. Li, E. P. A. M. Bakkers, and F. A. Zwanenburg, Electric-field dependent g -factor anisotropy in Ge-Si core-shell nanowire quantum dots, *Phys. Rev. B* **93**, 121408 (2016).
- [74] C. G. Van de Walle and R. M. Martin, Theoretical calculations of heterojunction discontinuities in the Si/Ge system, *Phys. Rev. B* **34**, 5621 (1986).
- [75] C. Wu, J.-P. Hu, and S.-C. Zhang, Exact SO(5) symmetry in the spin-3/2 fermionic system, *Phys. Rev. Lett.* **91**, 186402 (2003).
- [76] C. Kittel, *Quantum theory of solids* (Wiley, New York, 1963).
- [77] L. D. Landau and E. M. Lifshitz, *Quantum Mechanics* (Pergamon, New York, 1965).
- [78] E. N. Bulgakov and A. F. Sadreev, Spin polarization in quantum dots by radiation field with circular polarization, *Journal of Experimental and Theoretical Physics Letters* **73**, 505 (2000).
- [79] E. Tsitsishvili, G. S. Lozano, and A. O. Gogolin, Rashba coupling in quantum dots: An exact solution, *Phys. Rev. B* **70**, 115316 (2004).
- [80] Z. X. Wang and D. R. Guo, *Special Functions* (World Scientific, Singapore, 1989).
- [81] D. Csontos and U. Zülicke, Large variations in the hole spin splitting of quantum-wire subband edges, *Phys. Rev. B* **76**, 073313 (2007).
- [82] D. Csontos, U. Zülicke, P. Brusheim, and H. Q. Xu, Landé-like formula for the g factors of hole-nanowire subband edges, *Phys. Rev. B* **78**, 033307 (2008).
- [83] D. Csontos, P. Brusheim, U. Zülicke, and H. Q. Xu, Spin- $\frac{3}{2}$ physics of semiconductor hole nanowires: Valence-band mixing and tunable interplay between bulk-material and orbital bound-state spin splittings, *Phys. Rev. B* **79**, 155323 (2009).
- [84] P. C. Sercel and K. J. Vahala, Polarization dependence of optical absorption and emission in quantum wires, *Phys. Rev. B* **44**, 5681 (1991).
- [85] G. Fishman, Hole subbands in strained quantum-well semiconductors in [hkk] directions, *Phys. Rev. B* **52**, 11132 (1995).
- [86] L. Wang and M. W. Wu, Hole spin relaxation in p -type (111) GaAs quantum wells, *Phys. Rev. B* **85**, 235308 (2012).
- [87] I. A. Kokurin, Dimensional quantization and zero-field spin splitting of holes in GaAs nanowires, *Phys. Rev. B* **108**, 165301 (2023).
- [88] B. A. Bernevig, T. L. Hughes, and S.-C. Zhang, Quantum spin hall effect and topological phase transition in HgTe quantum wells, *Science* **314**, 1757 (2006).
- [89] X.-L. Qi and S.-C. Zhang, Topological insulators and superconductors, *Rev. Mod. Phys.* **83**, 1057 (2011).
- [90] M. A. Semina and R. A. Suris, Holes localized in nanostructures in an external magnetic field: g -factor and mixing of states, *Semiconductors* **49**, 797 (2015).
- [91] S. Bosco, M. Benito, C. Adelsberger, and D. Loss, Squeezed hole spin qubits in ge quantum dots with ultrafast gates at low power, *Phys. Rev. B* **104**, 115425 (2021).
- [92] F. N. M. Froning, M. J. Rancić, B. Hetényi, S. Bosco, M. K. Rehmann, A. Li, E. P. A. M. Bakkers, F. A. Zwanenburg, D. Loss, D. M. Zumbühl, and F. R. Braakman, Strong spin-orbit interaction and g -factor renormalization of hole spins in Ge/Si nanowire quantum dots, *Phys. Rev. Research* **3**, 013081 (2021).
- [93] A. P. Higginbotham, F. Kuemmeth, T. W. Larsen, M. Fitzpatrick, J. Yao, H. Yan, C. M. Lieber, and C. M. Marcus, Antilocalization of coulomb blockade in a Ge/Si nanowire, *Phys. Rev. Lett.* **112**, 216806 (2014).

- [94] F. N. M. Froning, L. C. Camenzind, O. A. H. van der Molen, A. Li, E. P. A. M. Bakkers, D. M. Zumbühl, and F. R. Braakman, Ultrafast hole spin qubit with gate-tunable spin-orbit switch functionality, *Nature Nanotechnology* **16**, 308 (2021).
- [95] F. K. de Vries, J. Shen, R. J. Skolasinski, M. P. Nowak, D. Varjas, L. Wang, M. Wimmer, J. Ridderbos, F. A. Zwanenburg, A. Li, S. Koelling, M. A. Verheijen, E. P. A. M. Bakkers, and L. P. Kouwenhoven, Spin-orbit interaction and induced superconductivity in a one-dimensional hole gas, *Nano Letters* **18**, 6483 (2018).
- [96] C. Kloeffer, M. Trif, and D. Loss, Acoustic phonons and strain in core/shell nanowires, *Phys. Rev. B* **90**, 115419 (2014).